

# Sidewall Electrodes in Microchannels for Dielectrophoretic Cell Separation and Electrochemical Detection

---

A

Thesis

Presented to

the faculty of the School of Engineering and Applied Science

University of Virginia

---

in partial fulfillment

of the requirements for the degree

Master of Science

by

XuHai Huang

May 2021

# APPROVAL SHEET

This  
Thesis  
is submitted in partial fulfillment of the requirements  
for the degree of  
Master of Science

Author: XuHai Huang

This Thesis has been read and approved by the examining committee:

Advisor: Nathan Swami

Advisor:

Committee Member: Mona Zebarjadi

Committee Member: James P. Landers

Committee Member:

Committee Member:

Committee Member:

Committee Member:

Accepted for the School of Engineering and Applied Science:



Craig H. Benson, School of Engineering and Applied Science

May 2021

# **Sidewall Electrodes in Microchannels for Dielectrophoretic Cell Separation and Electrochemical Detection**

**XuHai Huang**

## Abstract

Microfluidics in biological and medical research has gained much attention in the past decade for the purposes of separation and analysis of components within a complex sample. However, electrically functional microfluidic devices for biological sensing and cell manipulation require the ability to modulate electric field profiles over the channel width and depth, which is especially challenging to fabricate with minimum lithography steps. Metal deposition is the most ubiquitous method for integrating electrodes in microchannels, but the traditional deposition method is limited to planar electrodes, which have low electric field extents along the depth of the channel, thereby making them unsuitable for applications wherein sensing and manipulation are required over the channel depth. To address the need for uniform measurements over channel depth without highly specialized sidewall metal deposition steps, alternative electrode fabrication methods have been explored, such as conductive liquid electrodes, Ag-PDMS electrodes, and liquid metal electrodes. Current methods based on liquid electrodes have been limited by stability of the conductive fluid, whereas conductive polymer composites (Ag-PDMS) do not exhibit sufficient electrical conductivity for field coupling and liquid metal lacks physical stability for portable device applications. Here, we present the design principles for facile microfabrication to integrate liquid metal electrodes that solidify at room temperature, thereby enabling a microdevice for dielectrophoretic cell separation and electrochemical detection over the entire depth of the microchannel. Specifically, an electrode and sample channel are co-fabricated in a single lithography step and sequentially filled to enable electrically functional microfluidic separation and detection. Three distinct confinement approaches are examined for creating electrode channels that are physically separated from biological sample channels, but electrically coupled for enabling dielectrophoretic separation and electrochemical detection.

## **Acknowledgment**

I want to show my deepest appreciation to my advisor Nathan Swami for supporting me on this Master's work and giving me the opportunity to explore the rich field of microfluidics. I thank my committee members for reviewing the work presented here. I thank everyone in the Swami Lab for helping me get started in the lab and advising me every step of the way. I want to thank the ECE staff, faculties, and students for making my education and research progress smoothly.

Last but not least, I would like to thank my family and friends, especially my mother and father, for the support they have given me during my years of education. I thank my church family for being my backbone and keeping me grounded.

Nothing that's been written here or will be written hereafter would be made possible without my Lord Jesus Christ for allowing me to complete this work and keeping me on a path where I can work to honor Him.

# Table of Contents

<b>Chapter 1: Introduction .....</b>	<b>1</b>
1.1: Microfluidics .....	1
1.2: Electrically Functional Microfluidics .....	2
1.3: Dielectrophoresis .....	4
1.4: Electrochemistry .....	7
<b>Chapter 2: Device Design and Fabrication .....</b>	<b>9</b>
2.1: Confinement Methods .....	9
2.2: Microfluidic Fabrication .....	13
2.3: Fabrication Procedure .....	13
2.4: Soft Lithography .....	16
2.5: Metal Injection and Co-fabrication .....	18
2.6: Equipment and Material List .....	20
<b>Chapter 3: Dielectrophoretic Cell Separation .....</b>	<b>21</b>
3.1: Contactless Dielectrophoresis .....	21
3.2: Continuous Dielectrophoresis .....	26
3.3: Sidewall Electrodes COMSOL Simulation .....	28
3.4: Sidewall Electrodes Dielectrophoresis Validation .....	31
<b>Chapter 4: In Channel Electrodeposition and Electrochemistry .....</b>	<b>35</b>
<b>Chapter 5: Conclusion and Future outlook .....</b>	<b>38</b>

# List of figures

Figure 1: Clausius-Mossotti factor as a function of frequency for a model cell .....	5
Figure 2: Schematics of nDEP and pDEP .....	6
Figure 3: Schematics of contactless electrodes and recessed electrodes .....	9
Figure 4: Liquid metal electrodes by planar confinement .....	11
Figure 5: Liquid metal electrodes by depth confinement .....	12
Figure 6: Single layer SU-8 process flow .....	14
Figure 7: Multi-layer SU-8 process flow .....	15
Figure 8: Soft-lithography process flow .....	17
Figure 9: Field's metal injection process flow .....	19
Figure 10: PDMS devices with membrane confinement, planar confinement, and depth confinement Field's metal electrodes .....	19
Figure 11: PDMS cDEP devices with Field's metal electrodes .....	22
Figure 12: cDEP trapping concept .....	23
Figure 13: Schematic of cDEP's fluidics and electrical operations .....	24
Figure 14: cDEP with membrane confined Field's metal electrodes for pDEP trapping of macrophages .....	25
Figure 15. (a) Schematic of the orifice device .....	27
Figure 16: (a) Inverted microscope image of the orifice device active region .....	27
Figure 17: 3D Comsol simulation of electric field norm in planar and sidewall electrodes .....	29
Figure 18: Particle tracing simulation of nDEP in planar and sidewall electrodes .....	30
Figure 19: Orifice device DEP with RBCs .....	34
Figure 20: Microscope image of cross-section of the depth confined sidewall electrode .....	36
Figure 21: Schematic of gold electrodeposition on Field's metal in a microchannel .....	36
Figure 22: In channel electrochemistry for gold surface validation .....	37

# Chapter 1

## Introduction

### 1.1 Microfluidics

Microfluidics is the science and engineering involving manipulation and transport of fluids on a picoliter to microliter scale<sup>1</sup>. Microfluidic chip and lab-on-a-chip has become popular in biological and medical research due to its portability, speed, low sample volume requirements and its ability to be automated<sup>2</sup>. The advances in research and development of lab-on-a-chip have prompted its applications to be used in a point of care setting such as sample-in-answer-out systems. The most appealing aspect of microfluidics is its predictable and well controlled flow behavior. The small dimensions of the fluid channels ( $\sim 10\mu\text{m} - 1\text{mm}$ ) give rise to the laminar flow behavior which is a result of the low Reynolds number ( $Re$ ) shown in equation 1 where  $\rho$  is the density of the fluid,  $v$  is the flow velocity, and  $L$  is the characteristic linear dimension, and  $\mu$  is the dynamic viscosity of the fluid<sup>3</sup>.

$$Re = \frac{\rho v L}{\mu} \quad (1)$$

The laminar flow behavior in microfluidic devices proves to be essential for controlling the movement of particles such as cells within a microchannel as the particles follows the flow streamlines. Another aspect of laminar flow that is favorable is that hydrodynamic resistance within microchannels can be easily calculated to enhance fluidic designs. In addition, well controlled fluid flow, such as hydrodynamic focusing can control particle position within the microchannel. Having the ability to precisely control the particles' position is essential to cell enrichment techniques, since external forces can be localized, to cause acoustophoresis,

electrophoresis, and dielectrophoresis. Apart from well controlled particle movement, fluid mixing in the laminar regime occurs by diffusion only. Hence, schemes based on flowthrough electrochemical detection within a microchannel can quantify diffusivity of two or more chemical species.

## **1.2 Electrically Functional Microfluidics**

In recent years, coupling electrodes with microfluidics is highly attractive due to its sensitivity in single cell analysis<sup>4</sup>, cell separation<sup>5</sup>, and electrochemical detection<sup>6</sup>. However, electrode designs have been limited to planar electrodes wherein the electrodes are located at the bottom and / or the top of the microchannel. Planar electrode configurations have inhibited high throughput cell separation by dielectrophoresis (DEP) and limited optical imaging applications as the active region in a microchannel may be covered by the electrodes. In recent years, designs involving three-dimensional or sidewall electrodes in microchannels have emerged, but the fabrication of such electrode architectures has been challenging and limiting due to the need for highly specialized glancing deposition systems. This section will cover the advantages and disadvantages of planar electrodes, alternative three-dimensional or sidewall electrodes and outlook on such architectures.

Traditionally, planar electrodes, most commonly gold, are used in microfluidics due to its high stability and reproducibility. However, planar electrodes have a limited electric field extend along the depth of the channel, as it is typically located at the bottom of the microchannel. The limited field is suboptimal for flow through separation by DEP<sup>7</sup>, since the DEP force is proportional to the gradient of the electric field squared. Recent works involving flow through DEP separation are limited by the low throughput in cell/particle numbers, which is apparent by the low flow rates in such applications<sup>8</sup>. To compensate for the low field extent, microfluidic channels with sawtooth

constriction designs along the length of the microchannel have been explored to enhance field<sup>9</sup>. However, constrictions in microchannel are prone to clogging from debris and aggregated cells, which are not suitable for samples with high cell/particle concentrations.

Facile co-fabrication strategies<sup>10</sup> have emerged, wherein multiple adjacent microchannels with different functionalities are formed in a single layer. Co-fabrication has led to the realization of so-called electrode channels<sup>11</sup>, wherein conductive substances are injected into microchannels to form electrodes. This method of fabrication creates three dimensional electrodes that extends over the entire depth of the microchannel. Two popular conductive substances used as electrodes are 10X Phosphate-buffered Saline<sup>11</sup> (10X PBS) and silver PDMS<sup>12</sup> (Ag-PDMS) due to their easy integration; as both methods can be performed with purchased materials in a cleanroom free environment. However, an inhibiting factor for 10X PBS and Ag-PDMS to be an effective electrode material for flowthrough DEP is their low conductivity of  $\sim 120\text{mS/cm}$  and  $\sim 50\text{S/cm}$ , respectively. Hence, voltage drops in the electrode channel limit the delivered voltage to the sample channel.

An alternate electrode material that has been explored using co-fabrication technique is liquid metal. A popular liquid metal is eutectic gallium indium (EGaIn)<sup>13</sup> which is a liquid metal at room temperature, therefore it can be easily injected and manipulated inside a microchannel. Though, EGaIn overcomes the low conductivity issue, its liquid state at room temperature is prone to deformation and limits the ability for surface modification, such as electrodeposition of a metal layer or self-assembled monolayer.

Another material that has gain much attention is Field's metal (FM). Unlike EGaIn, Field's metal is a low melting alloy composed of 51% indium, 32.5% bismuth, and 16.5% tin that is solid at room temperature and has a melting point of  $62.5\text{ }^\circ\text{C}$ . Liquid Field's metal is viscous and has high

surface tension due to the oxide on its surface. By heating the Field's metal to its melting point, the viscous liquid metal can be injected into microchannels and allowed to solidify at room temperature, forming solid metal electrodes. The solid architecture of the metal electrodes opens a plethora of novel application, such as high throughput DEP applications, in-channel electrodeposition, and electrochemical sensing. Furthermore, rapid fabrication of such electrodes leads to highly reproduceable, shelf-stable and cost effective electrically functional microfluidics for commercialization.

### 1.3 Dielectrophoresis

Dielectrophoresis (DEP) is a phenomenon wherein polarizable particles experience a translational force under a spatially non-uniform electric field<sup>14</sup>. DEP has gained much attention for its application in label-free separation of cells based on their inherent electrophysiology. This method of cell enrichment is of much interest due to its high sensitivity in differentiating cell subpopulation, based on their polarizability<sup>15</sup>, without labeling the sample, which can result in selection bias.

To understand a particle's motion caused by DEP we must look at the DEP force,  $F_{DEP}$ , equation expressed in equation 2 where  $\epsilon_m$  is the permittivity of the media,  $r$  is the radius of the particle,  $CM$  is the real part of the Clausius-Mossotti factor, and  $\nabla E^2$  is the Laplacian operator acting of the electric field squared<sup>14</sup>.

$$F_{DEP} = 2\pi\epsilon_m r^3 CM \nabla E^2 \quad (2)$$

Based on this equation, particles with a different radius experience a different level of DEP force therefore enabling size-based separation in a heterogenous population. A particle can be described as experiencing negative DEP (nDEP), figure 1 (a), where the particle moves away from the high

field point due to the polarization of the medium or positive DEP (pDEP), figure 1 (b), where the particle moves towards the high field point due to polarization of the particle.

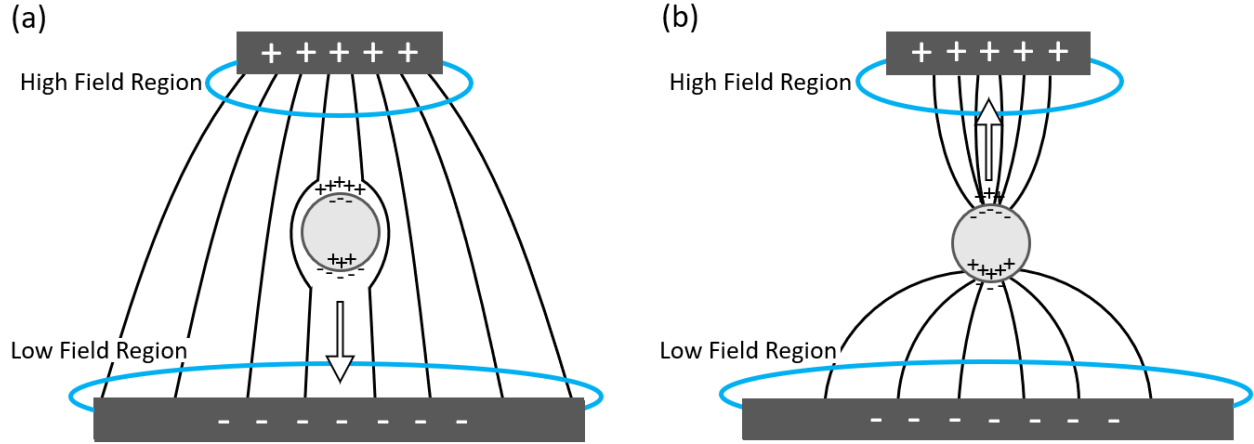


Figure 1: Schematics of (a) nDEP and (b) pDEP

However, the more powerful aspect of DEP is its ability to separate similar-sized particles based on their polarizability, which is described by the Clausius-Mossotti factor. The Clausius-Mossotti factor, equation 3, can be expanded to show the relationship between the dielectric properties of the particle,  $\epsilon_p$ , and its surrounding medium,  $\epsilon_m$ .

$$CM = \left( \frac{\epsilon_p - \epsilon_m}{\epsilon_p + 2\epsilon_m} \right) \quad (3)$$

However, for AC applications where the particles are cells and the surrounding medium is a conductive electrolyte, then it is important to consider the complex permittivity of the particle,  $\epsilon_p^*$  and surrounding medium,  $\epsilon_m^*$ , expressed in equation 4 where  $\epsilon_0$  is the permittivity of free space,  $j$  is  $\sqrt{-1}$ ,  $\sigma_p$  and  $\sigma_m$  is the conductivity of the particle and media.

$$\epsilon_p^* = \epsilon_0 \epsilon_p - \frac{j\sigma_p}{2\pi f} \quad \text{and} \quad \epsilon_m^* = \epsilon_0 \epsilon_m - \frac{j\sigma_m}{2\pi f} \quad (4)$$

From the above equation, the CM can be rewritten in its complex form, equation 5, and the  $F_{DEP}$  can also be rewritten to include a frequency component, equation 6<sup>16</sup>, where  $Re(f_{cm})$  is the real part of the Clausius-Mossotti factor as a function of frequency.

$$CM = \left( \frac{\epsilon_p^* - \epsilon_m^*}{\epsilon_p^* + 2\epsilon_m^*} \right) \quad (5)$$

$$F_{DEP} = 2\pi\epsilon_m r^3 Re(f_{cm})(\nabla E^2) \quad (6)$$

With the additional frequency dependency, the Clausius-Mossotti factor becomes critical in determining the direction of the particle's motion, wherein a positive Clausius-Mossotti factor results in the field polarizes the particle, thus pDEP and a negative Clausius-Mossotti factor results in the field polarizing the media around the particle, thus nDEP. To better visualize the Clausius-Mossotti factor, MyDEP software was used to plot the Clausius-Mossotti factor as a function of frequency for a model particle, such as a red blood cell (RBC) in a hypothetical medium with conductivity of 500 $\mu$ s/cm, figure 2.

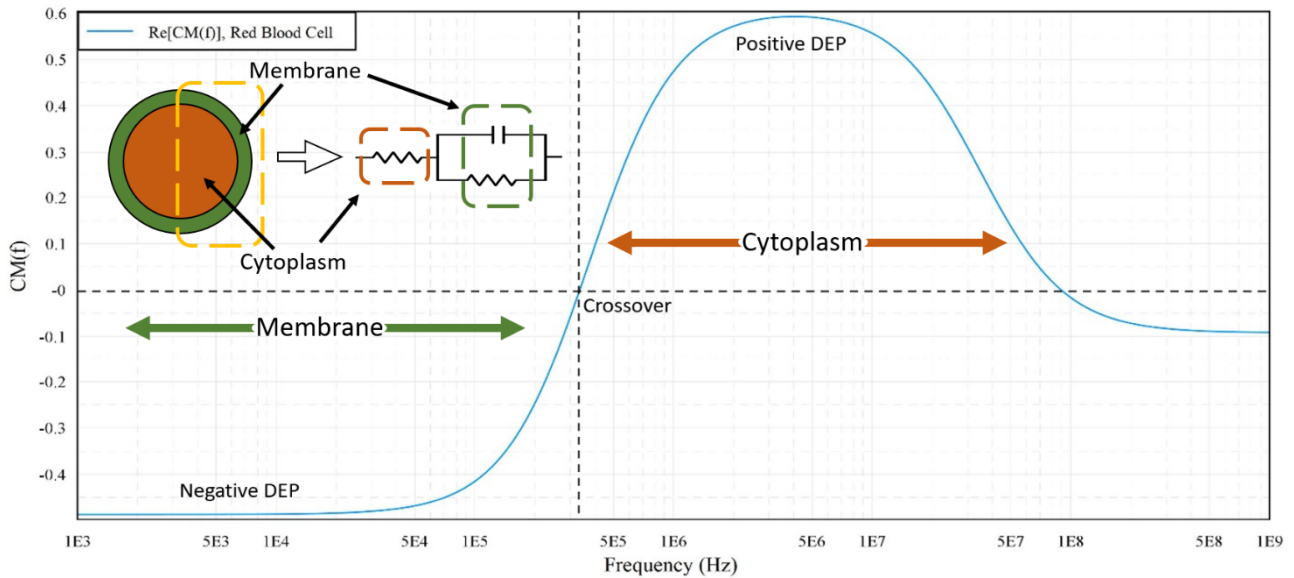


Figure 2: Clausius-Mossotti factor as a function of frequency for a model cell in medium with conductivity of 500 $\mu$ s/cm

A simplified shell modeling of a cell as circuit elements is shown in figure 2, wherein the cell membrane is modeled by a capacitor in parallel with a resistor and the cell cytoplasm is modeled by a resistor in series with the membrane lumped element. As seen in the Clausius-Mossotti factor as a function of frequency in figure 2, a particle under the application of a low frequency AC field results in a negative Clausius-Mossotti factor wherein the cell membrane is screening the field therefore nDEP and while a particle under a high frequency AC field results in a positive Clausius-Mossotti factor wherein the field bypasses the membrane and polarizes the cytoplasm therefore pDEP. Hence, particles or cells of different dielectric properties in a medium of fixed dielectric constant can be deflected towards or away from the high field region based on the frequency of the applied electric field enabling frequency selective separation.

## **1.4 Electrochemistry**

As the field of chemical sensors namely electrochemical sensors and detectors grows, there has been a major interest in miniaturizing electrochemical sensors with microtechnology and integration of electrochemical sensors into microfluidic platforms<sup>17</sup>. The traditional microfluidic devices with electrochemical sensors consist of planar gold working electrodes at the bottom of the bottom of the microchannel. The advantage of such an electrode architecture is the high electrode purity and fabrication reproducibility, however, planar electrodes are not suitable in applications where sensing along the depth of the microchannel is required. Furthermore, planar electrode devices do not fully utilize microfluidics' flow focusing ability, wherein species can be modulated within the microchannel to study diffusivity along the length of the microchannel. Furthermore, integrating sidewall sensing electrodes flanking a microchannel would allow for sensing across and along the depth of the microchannel. As discussed in prior sections, traditional fabrication methods for metal side wall electrodes are highly specialized and therefore limiting its

use. In addition, electrode material for electrochemical sensors is limited to materials with well-known oxidation and reduction behaviors, therefore existing sidewall electrodes made from liquid metal or low melting alloy is not suitable for such applications.

# Chapter 2

## Device Design and Fabrication

### 2.1 Confinement Methods

As mentioned, prior, there is a plethora of microfluidics applications enabled by solid three-dimensional sidewall metal electrodes integrated with microchannels. Herein, we present two novel in-channel sidewall metal electrode designs and their fabrication techniques. In addition, we demonstrate the possibility of using Field's metal as an alternative electrode material in a microfluidic contactless dielectrophoresis chip.

Sidewall electrodes in prior works were created as: (a) contactless electrodes, figure 3 (a), wherein the electrodes are separated by a physical insulative membrane from the sample channel<sup>11</sup> or (b) recessed contact electrodes, figure 3 (b), wherein the electrodes are recessed but inside the sample channel<sup>18</sup>.

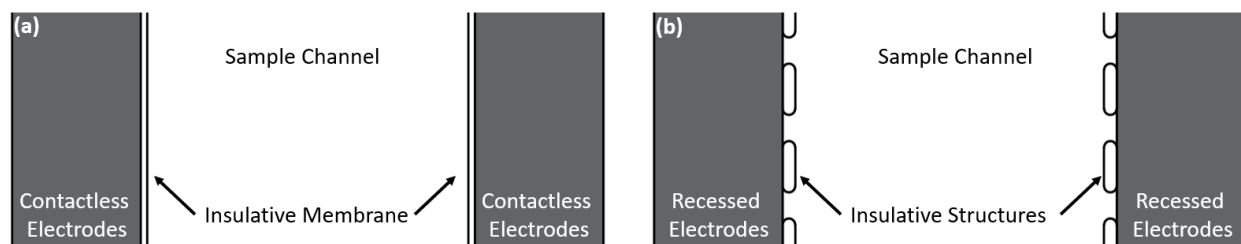


Figure 3: Schematics of (a) contactless electrodes and (b) recessed electrodes

The benefit of an isolated electrode is the reduced contamination in the sample channel and reduced influence on cell viability<sup>19</sup> during application of electric field. However, an insulative barrier creates a significant voltage drop between the applied voltage and the stimulating voltage, which can be calculated as the voltage fraction for stimulation<sup>20</sup>. In contrast, recessed contact

electrodes can deliver voltage directly to the sample channel, but the electrode materials are limited to ones that can be self-contained in the electrode channel such as elastic composites or viscous liquids. A common solid electrode material is Ag-PDMS, which is a conductive composite made by mixing micro sized silver particles with uncross linked PDMS<sup>21</sup>. This method of electrode fabrication is popular due to its low cost, but the electrodes are highly insulative and viscous. The high viscosity is derived from the high silver volume percentage which makes the material difficult to integrate into microchannels. Unlike Ag-PDMS, liquid metals or low melting alloys is highly conductive and be easily injected into microchannels to act as either contact or contactless electrodes.

Prior works have used liquid metal as contact electrodes made from a co-fabrication strategy by taking advantage of its viscosity and high surface tension to confine the liquid metal in the electrode channel by an array of posts<sup>13</sup>. Despite the simplicity and cost effectiveness of using such metals as sidewall electrodes in a microchannel, liquid metal has not been study extensively for DEP applications, due to the challenges associate with the creation of non-uniform electric fields. Furthermore, to remove variations from focusing position of particles in the channel, sequential DEP translation along the length of the microchannel is preferred for progressive deflection of particles traveling along the microchannel. For this purpose, the spatial non-uniformity must extend uniformly over the entire device depth. Here we present a strategy to create sequential field non-uniformities using a set of sidewall metal electrodes.

The principle to confining liquid metal in a microchannel with an opening is by designing the opening with a critical dimension such that the pressure required to inject the liquid metal into the opening is double of the pressured required to inject it along the channel<sup>13</sup>. Within such design, the liquid metal follows the path of least resistance, “injection path” in figure 4 (a), along the electrode channel while the posts/opening are the high resistance path, thereby containing the liquid metal. In this study, Field’s metal was chosen as the electrode material since it is a solid at room temperature, but liquid at 65 °C. A critical dimension of 35 $\mu\text{m}$  was determined experimentally for liquid FM when the injecting path was 1000 $\mu\text{m}$  in width. Therefore, using a set of 25 $\mu\text{m}$  posts separated by 35 $\mu\text{m}$  edge to edge spacing figure 4 (b), the liquid Field’s metal can be confined to the electrode channel with a high degree of reproducibility.

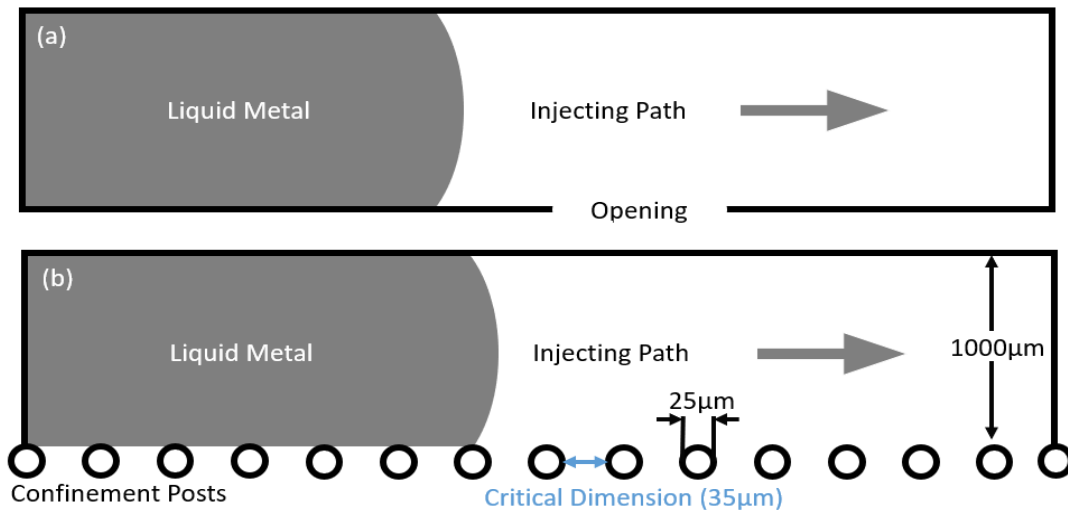


Figure 4: (a) Liquid metal injection in a microchannel. (b) Planar confinement of liquid Field’s metal by posts separated by a critical dimension

Using posts to confine the liquid FM was sufficient to act as “ground” electrode since the exact surface area of the electrode is not important. However, for electrodeposition of a gold overlayer for electrochemical sensing, uniformity of the electrode surface area is of utmost importance. Hence, we present a novel design to confine the Field’s metal for a more uniform electrode profile in the microchannel. The confinement principle is similar to that with the posts and the orifices, but instead of creating confinement in a planar manner, x-y plane of figure 4 (a and b), the geometry presented here creates the confinement in the z-y plane, which we call depth confinement, figure 5, as opposed to planar confinement in the previous case. This form of confinement was realized by creating a step height difference between the sample channel and the electrode channel. In this manner, arbitrary long uninterrupted electrodes can be made to flank the sample channel with a well-defined exposed surface such that the active surface area can be calculated to a high degree of certainty.

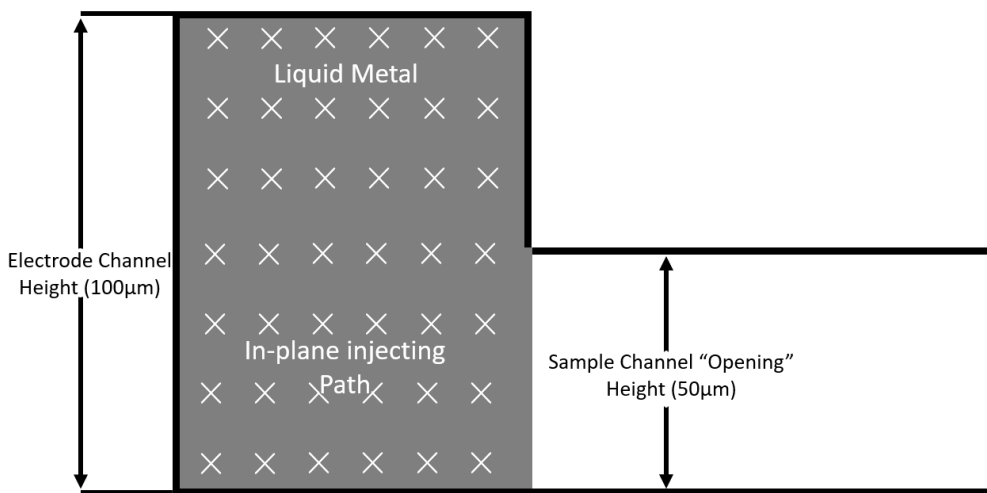


Figure 5: Depth confinement of liquid Field’s metal by step height between the electrode and sample channel.

## 2.2 Microfluidic Fabrication

The most common material used in microfluidic devices is Polydimethylsiloxane<sup>15</sup> (PDMS) due to its low cost and ease for prototyping. The main advantage of PDMS that made it popular within the biomedical community is its optical transparency and biocompatibility; these two criteria allow for applications involving biological samples and optical imaging inside the channel. Apart from PDMS, another material with similar properties is the thermal plastic cyclic olefin copolymer (COC). However, COC have not been a mainstream prototyping material in research labs for its complicated fabrication methods involving hot embossing or injection molding that are rarely used in academia.

PDMS is a biostable, nontoxic, and flexible elastomer<sup>16</sup> used predominantly in micromolding, also known as soft lithography, wherein uncrosslinked PDMS is poured over a master mold and allowed to crosslink or cure on a hot plate to form the inverse of the master mold. The master mold used in this study for micromolding was made from SU-8, a high aspect ratio negative photoresist, on a silicon wafer by standard photolithography. Contrary to the positive photoresist used in semiconductor fabrication, SU-8 is crossed linked by UV. 3D printed micromolds were also explored, but the surface roughness from the 3D printed micromolds transferred to the PDMS and made it unsuitable for applications with small (<10 $\mu$ m) feature size.

## 2.3 Fabrication Procedure

SU-8 photoresist was used in this study to create the master mold by standard photolithography. A layer of SU-8 was spun onto a 4-inch silicon wafer to form a 50 $\mu$ m thick film followed by a soft baking process to remove residual solvent from the SU-8. After soft baking, the wafer was allowed to cool to room temperature before UV exposure using a photomask to form the negative features.

A post exposure bake was carried out followed by a development step using SU-8 developer to remove the uncrosslinked SU-8. To finalize the master mold, the silicon wafer with SU-8 was hard baked to fully crosslink the features. A sample process flow for SU-8 master mold is shown in figure 6.

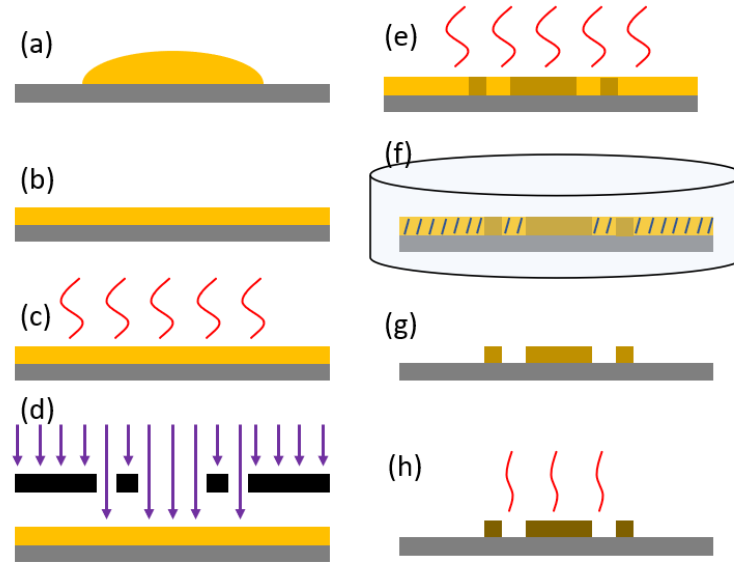


Figure 6: Complete process flow for SU-8 master mold. (a,b) Spinning of SU-8 (yellow) at 3000RPM. (c) Soft bake at 95 °C for 20 minutes. (d) UV exposure at a constant dosage of 165mJ/cm<sup>2</sup>. (e) Post exposure bake at 95 °C for 7 minutes. (f) SU-8 development in SU-8 developer for 15 minutes. (g) Example of pre-hard bake wafer. (h) Hard baking at 150 °C for 30 minutes.

The process described above is to create single layer master molds for PDMS chips that are suitable for planar confinement of FM. However, single layer master molds and PDMS chips cannot create depth confinement of the FM, as depth confinement requires a step height difference and single layer SU-8 is only able to achieve structures of the same height. To create the step height geometry, multilayer SU-8 fabrication was carried out. Multilayer SU-8 is similar to the single layer process flow, except the wafer is not developed following the first exposure step. Instead, another layer of 50µm thick SU-8 film was spun onto the original wafer directly after the post exposure bake

step. The wafer is then soft baked and exposed again. A unique aspect to multilayer SU-8 is the carefully designed exposure energies, since the first exposure, on the 50 $\mu\text{m}$  layer, should be lower than the typical energy used for single 50 $\mu\text{m}$  thick layer processes and the second exposure, on the 100 $\mu\text{m}$  (first and second layers combined) thick layer, should be higher than single 100 $\mu\text{m}$  layer processes to accommodate for the reduced energy in the first exposure step. In addition to the careful exposure energy design, precise mask alignment during the second exposure is crucial to create well defined features. The complete process flows for multilayer SU-8 master mold fabrication is shown in figure 7.

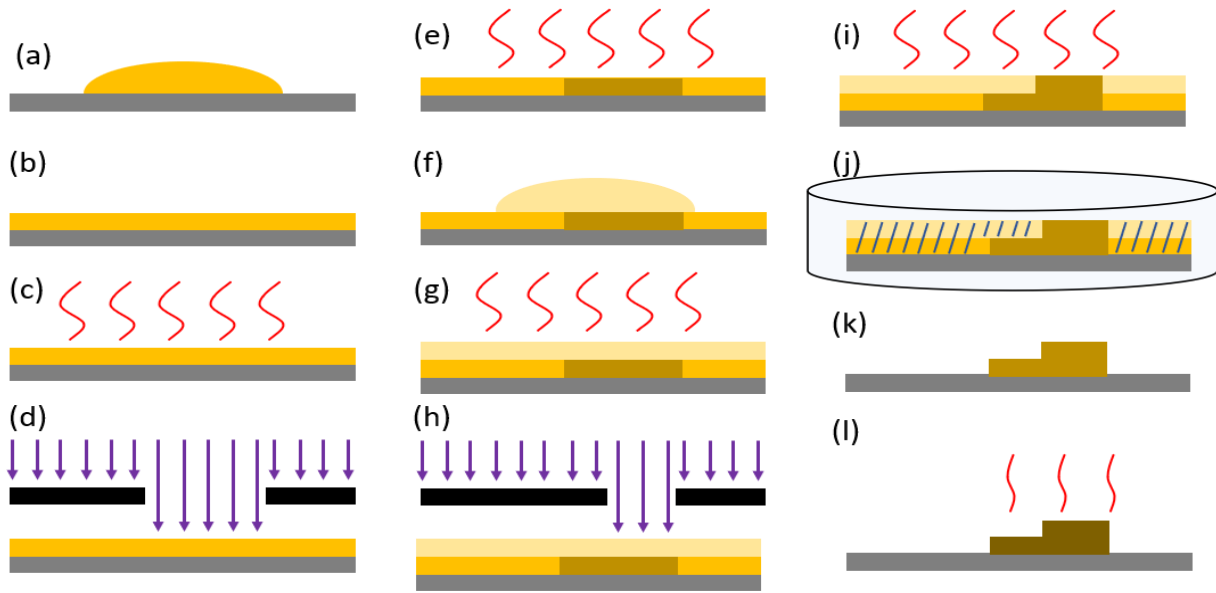


Figure 7: Complete process flow for multilayer SU-8 master mold. (a,b) Spinning of first layer SU-8 (yellow) at 3000RPM. (c) Soft bake at 95 °C for 20 minutes. (d) UV exposure at a constant dosage of 145mJ/cm<sup>2</sup>. (e) Post exposure bake at 95 °C for 7 minutes. (f) Spinning of second layer SU-8 (light yellow) at 3000RPM. (g) Soft bake at 95 °C for 20 minutes. (h) UV exposure at a constant dosage of 265mJ/cm<sup>2</sup>. (i) Post exposure bake at 95 °C for 10 minutes. SU-8 development in SU-8 developer for 20 minutes. (g) Example of pre-hard bake wafer. (h) Hard baking at 150 °C for 30 minutes.

## 2.4 Soft Lithography

Soft lithography or micromolding is a pattern transferring technique<sup>17</sup> where features from a master mold are cast into a soft material such as PDMS. As mentioned previously, PDMS is an elastomer which requires a crosslinking process, therefore, uncrossed linked PDMS can be easily poured over the master mold formed from SU-8 and crossed linked on a hot plate to form the positive features. Cross linked PDMS with the features can then be either bonded to featureless PDMS or glass to form complete microchannels.

Prior to micromolding, the SU-8 master mold was silanized with Trichloro silane to enhance the releasing of crosslinked PDMS from the master mold. A 5:1 PDMS base to PDMS crosslinker was used for micromolding in this study. PDMS base and crosslinker were mixed by hand at room temperature for 5 minutes and off gassed in a desiccator for 15 minutes. The off gassed mixture was poured over the SU-8 master mold and off gassed again for another 15 minutes to ensure the PDMS is casted into the SU-8 without the presence of bubbles. Following the second off gassing step, the PDMS and substrate were placed on a hot plate to crosslink. The crosslinked PDMS was released from the SU-8 by carefully peeling the PDMS from the substrate. A biopsy punch was used to create the inlet and outlet of the microchannel. The PDMS chip was then bonded to a glass slide by plasma bonding. Both the chip and the glass slide were placed in a plasma clearer for 30 seconds at 20 W power to create OH groups on the surface of PDMS chip and glass slide; the two pieces were stacked with the glass slide acting as the substrate. The completed chip was place on hot plate at 95 °C for 5 minutes to enhance the bonding strength.

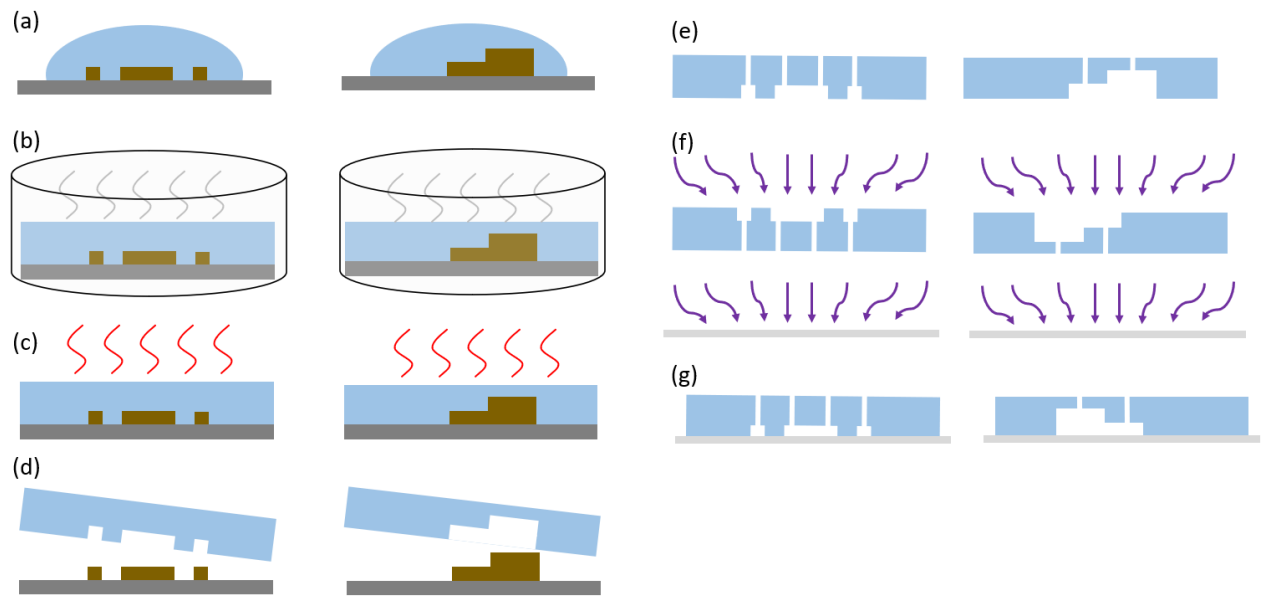


Figure 8: Complete process flow for PDMS micromolding. (a) Pouring off gassed PDMS onto SU-8 master mold substrate. (b) Second off gassing step in desiccator for 15 minutes. (c) PDMS curing on a hotplate at 60 °C for 12 hours. (d) Peeling the cross linked PDMS from the substrate. (e) Channel inlets and outlets were made with biopsy punches. (f,g) Plasma bonding of PDMS to glass.

## 2.5 Metal Injection and Co-fabrication

As described above, a co-fabrication strategy was used to form the metal sidewall electrodes wherein liquid Field's metal was injected into the PDMS microchannels by a syringe. By using the co-fabrication method, the liquid metal self-aligns itself along the microchannel, therefore eliminating any labor-intensive alignment steps. Three electrode confinement geometries were studied: membrane confinement, planar confinement, and depth confinement. All three devices were made from PDMS with the same process listed in the previous section.

Prior to metal injection, the PDMS chips were placed in a desiccator partly submerged in water to create a humid environment to increase the wettability of the PDMS channels. This wetting step is typically done for 5-10 minutes depending on the size of the desiccator. A piece of FM was melted using a hot air gun until it is fully liquefied. The liquid FM was loaded into a modified pipet tip attached to a 1mL syringe by apply sufficient negative pressure to draw 100uL from the pool of liquid FM. The syringe was cooled to room temperature allowing the liquid metal to solidify before attaching it to the electrode channel inlets on the PDMS chip. It's important that the syringe piston starts at 0.5 mL before withdrawing the liquid metal; the extra 0.5 mL of air within the syringe is necessary to provide additional positive pressure during injection. Prior to submerging the PDMS chip along with the metal filled syringe(s) into a 65 °C water bath, electrode channel outlet extension(s) were made using plastic tubing while sample channel inlet(s) and outlet(s) were plugged to prevent water from entering the microchannels. The entire system was then submerged for in the water bath for 1 minute for the solid FM to melt. Following, ~13kPa<sup>9</sup> positive pressure was applied to the syringe(s) until the electrode channels were filled. Once the liquid metal fills the electrode channel(s), the applied pressure was halted allowing the excess pressure to continue filling the electrode channel extension(s). Once the residual liquid metal in

the electrode channel extension(s) solidifies, the entire system was removed from the water bath and cooled to room temperature for the liquid metal to solidify in the microchannels. Excess electrode channel extension(s) and electrode inlet pipet(s) were cut with pliers and wires were soldered to create the electrical interface. The process flow for Field's metal injection is found in figure 9. Final channel images of the three confinement methods are shown in figure 10.

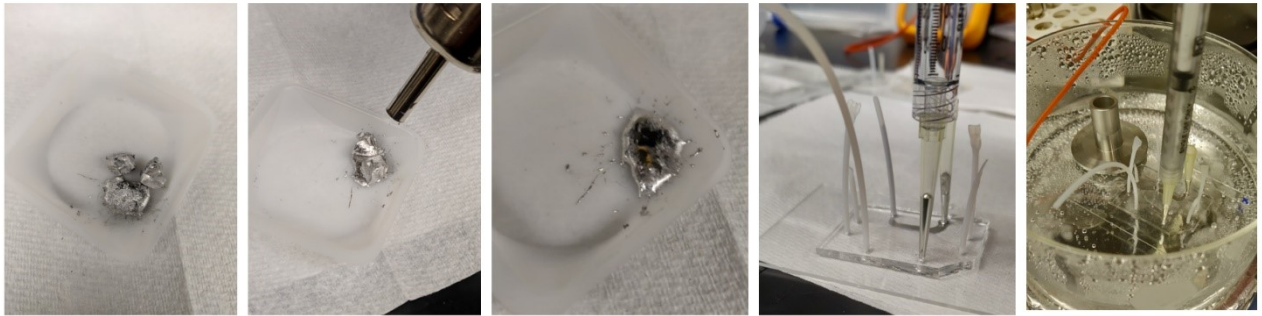


Figure 9: Field's metal injection process flow

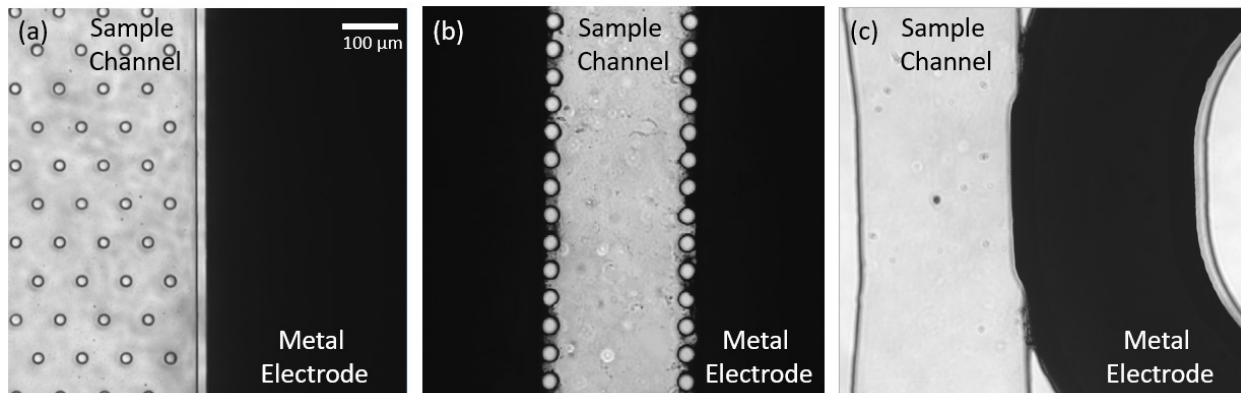


Figure 10(a) Membrane confinement where the metal is physically separated from the sample channel with an insulative barrier. (b) Post to post confinement (posts are designed with a critical separation) and (c) step height confinement (designed with a critical step height) so that the metal is in direct contact with the sample channel but maintained in the electrode channel due to its high surface tension.

## 2.6 Equipment and Material List

The master molds were fabricated from SU-8 3050 photoresist (Kayaku Advanced Materials) on 4-inch silicon wafers from University Wafer, Inc. Photomasks were designed with AutoCAD and printed on a chrome on soda lime photomask ordered from Photo Sciences, Inc. Both the UV exposure and photomask alignment step(s) were done with a EVG 620 mask aligner (EV Group). SU-8 developer from Kayaku Advanced Materials was used for the development step. The silane used to treat the surface of the SU-8 master mold was Trichloro (1H,1H,2H,2H-perfluorooctyl) silane 97% from Sigma-Aldrich. Sylgard<sup>TM</sup> 184 PDMS base and PDMS crosslinker from DOW Corning was used for micromolding/soft lithography. The glass slide for bonding to the PMDS bonding was Fisherbrand<sup>TM</sup> plain glass microslides from Thermo Fisher Scientific. The plasma bonding was done with the Tergeo Plasma System (Pie Scientific). The Field's metal was bought from RotoMetals.

## **Chapter 3**

# **Dielectrophoretic Cell Separation**

Dielectrophoretic cell separation is commonly used to selectively isolate and enrich cell subpopulations for cells that lack reliable surface markers. DEP applications have emerged in both static and dynamic DEP. Static DEP is most commonly found in devices with microwells<sup>22</sup> for cell separation or cell characterization. However, static DEP is not suitable for high-throughput cell separation therefore, much interest has been placed in microfluidics that couples fluid flow with DEP to enable batch and continuous DEP separation<sup>23</sup>. Two DEP separation devices are examined here, one based on a batch separation process while the other based on a continuous separation process.

### **3.1 Contactless Dielectrophoresis**

Contactless dielectrophoresis (cDEP) is a method wherein cells are never in direct contact with the electrode material. This method of separation is especially useful in situations with delicate cell types, such as rare cancer or stem cells that are prone to cell death by contamination or electrical lysis. However, a significant drawback of cDEP microfluidic devices is the difficulty in fabrication and the poor reproducibility due to using a conductive liquid (10X PBS) as the electrode. A cDEP device is comprised of a sample channel and two electrode channels flanking the sample channel separated by an insulative membrane. For optimal DEP response, the insulative membrane is designed to be as thin as the polymer material allows ( $\sim 15\mu\text{m}$ )<sup>7</sup>, so that maximum electric field can pass through the membrane. Since the electrode material used in such devices is 10X PBS, any imperfection in the membrane results in the 10X PBS leaking from the electrode channel into the sample channel, rendering the device faulty.

To overcome the delicate membrane fabrication problem, alternative electrode materials were studied such as Ag-PDMS and Field's metal (FM). Ag-PDMS was a promising electrode material, however, it was not suited for such an application since the uncured Ag-PDMS was too viscous to integrate into the electrode channels without breaking the membrane. Instead of Ag-PDMS, FM was used as the alternative electrode material, wherein the Field's metal was melted and injected into the isolated electrode channels while the device is submerged in a water bath. After removing the device from the water bath and cooled to room temperature, the liquid FM inside the electrode channels would solidify creating isolated metal electrodes, figure 11 (a). Due to the high viscosity of liquid FM, imperfections in the membrane would not render the device useless, as the metal is still contained within the electrode channel, figure 11 (b). In fact, up to 70 $\mu$ m long defects in the membrane could be recovered. Besides overcoming the membrane imperfection, the solid FM also acts as a structural reinforcement to the membrane, so that the device is more robust during operation.

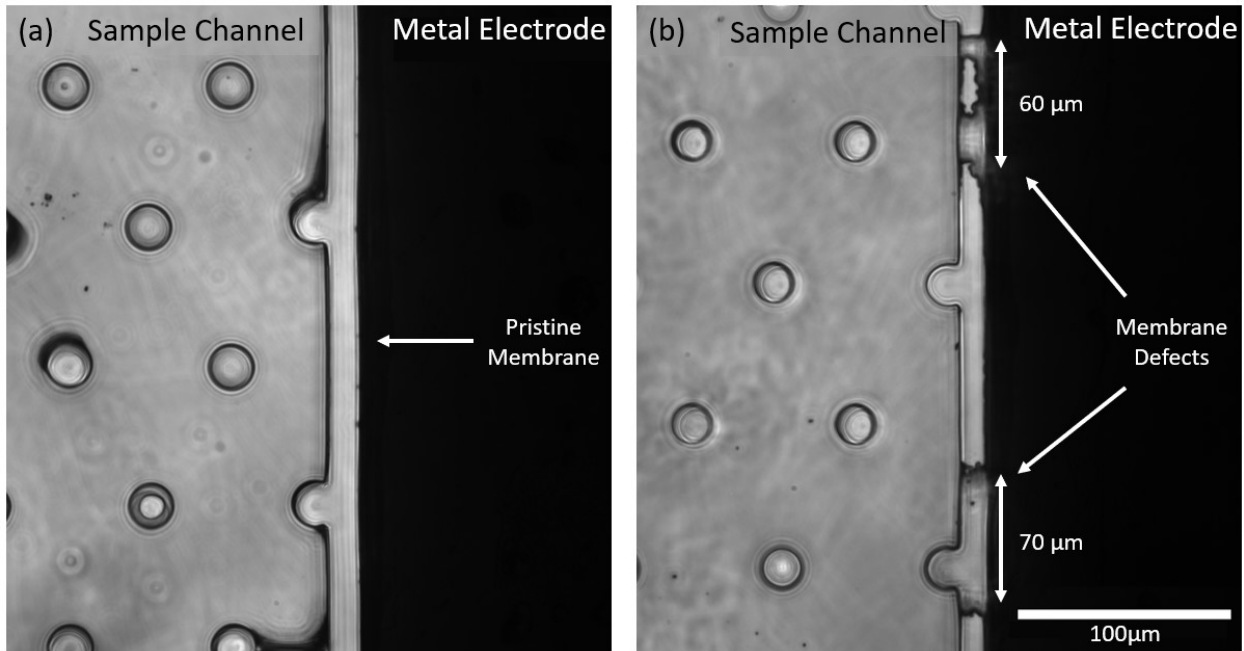


Figure 11: PDMS cDEP devices with electrodes replaced with Field's Metal. (a) Pristine membrane. (b) Membrane with defects.

Contactless DEP devices operate in a batch separation mode, wherein cells are trapped to arrays of insulative posts in the sample channel by pDEP. The insulative posts disrupts the electric field and creates a localized field non-uniformity around the posts, with the high field points located at post region that is tangential to the electric field direction and perpendicular to the fluid flow direction, figure 12 (a and b). In this manner, cells that are expected to exhibit pDEP are attracted and trapped at the posts when it is within the localized field non-uniformity.

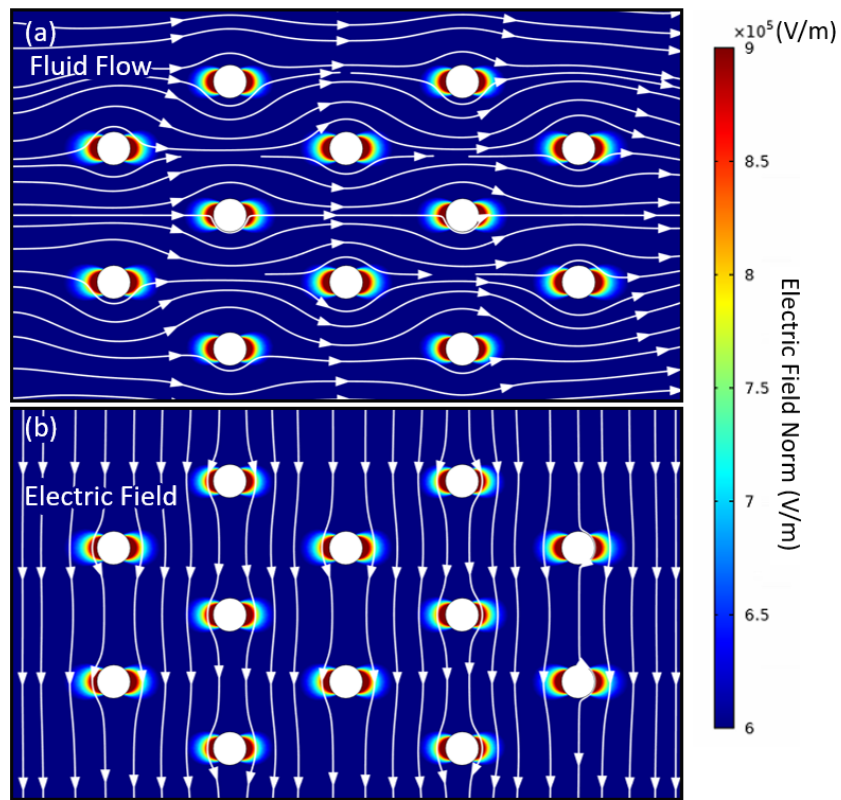


Figure 12: cDEP operation concept. (a): fluid flow direction (b): electric field direction. Color surface to show the high field point (red) around the posts.

To test the operation of FM cDEP devices, DEP trapping of mouse derived macrophages was examined. The macrophages were removed from its culture media, washed three times and resuspended in a DEP buffer, composed of: 8.6% sucrose, 0.3% glucose, 0.1% BSA, and 1XPBS that is adjusted to a conductivity level of  $25\mu\text{S}/\text{cm}$ . Prior to loading sample into the cDEP device,

the sample was diluted to a cell concentration of  $5 \times 10^5$  cell/mL to prevent clogging and the buffer conductivity was validated with a conductivity meter by three independent measurements.

Two syringe pumps were used to fill and load the macrophage sample into the sample channel of the cDEP device. One syringe (buffer syringe) was used solely to fill the sample channel with the DEP buffer, while the other syringe (sample syringe) was used to load the sample, figure 13.

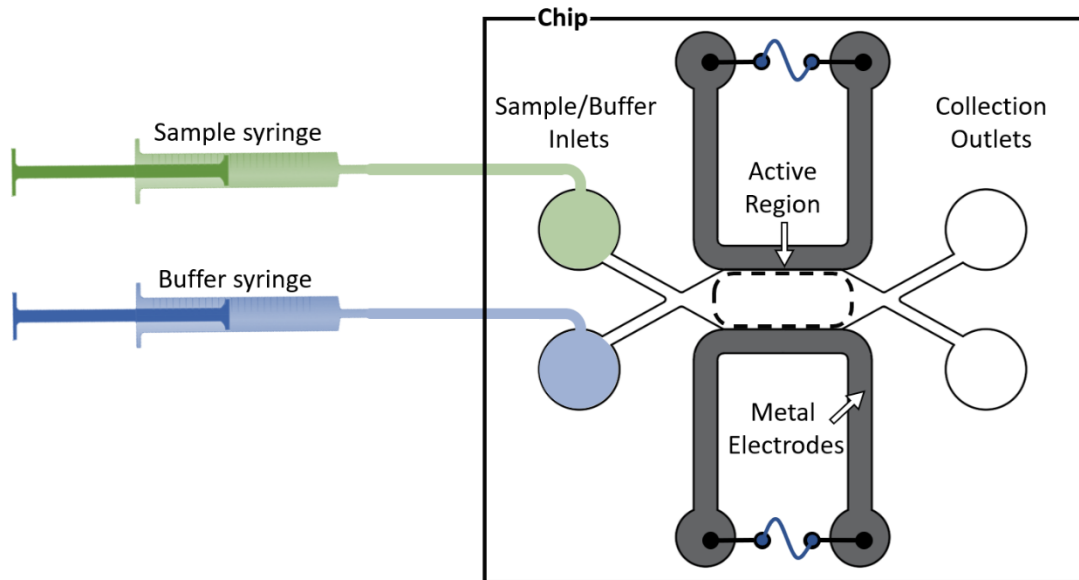


Figure 13: Schematic of cDEP's fluidics and electrical operations

Once, the channel was sufficiently filled with the DEP buffer, the buffer syringe was disconnected from the device and replaced with the sample syringe to load the macrophage sample. After loading the sample, the syringe pump was turned off, so that the macrophages in the sample channel were only moving under inertia. A function generator coupled with an amplifier, was used to deliver  $400V_{pp}$  to the system for DEP trapping. A frequency sweep was performed starting from 10kHz until strong pDEP trapping at 80kHz at a constant  $400V_{pp}$ . During the frequency sweep, onset pDEP, “clinging”, was observed at 25kHz and pDEP trapping was observed at frequencies greater than 50kHz. However, strong pDEP trapping was only seen at 80 kHz. To verify that the trapping

at  $400V_{pp}$  at 80kHz is due to the dielectrophoretic force, images of the sample channel were taken prior to trapping, during trapping, and after releasing, as shown in figure 14. Figure 14 (a) was taken 1 second before applying voltage where the macrophages, circled in red, are moving due to inertial forces. Upon applying  $400V_{pp}$  at 80kHz, the macrophages, circled in green, are trapped to nearby post, colored in blue, figure 14 (b). Another image was taken after 2 seconds after the voltage was turned off figure 14 (c) where the macrophages, in orange, are released from the posts they were trapped to, colored in blue, and moving away by inertial forces similar to what was seen before trapping. By tracking the movements of the macrophages and marking the posts they were trapped to, we therefore, confirm the trapping mechanism is by DEP, as no other forces in the system can exhibit this type of trapping under voltage ON conditions, and releasing under voltage OFF conditions.

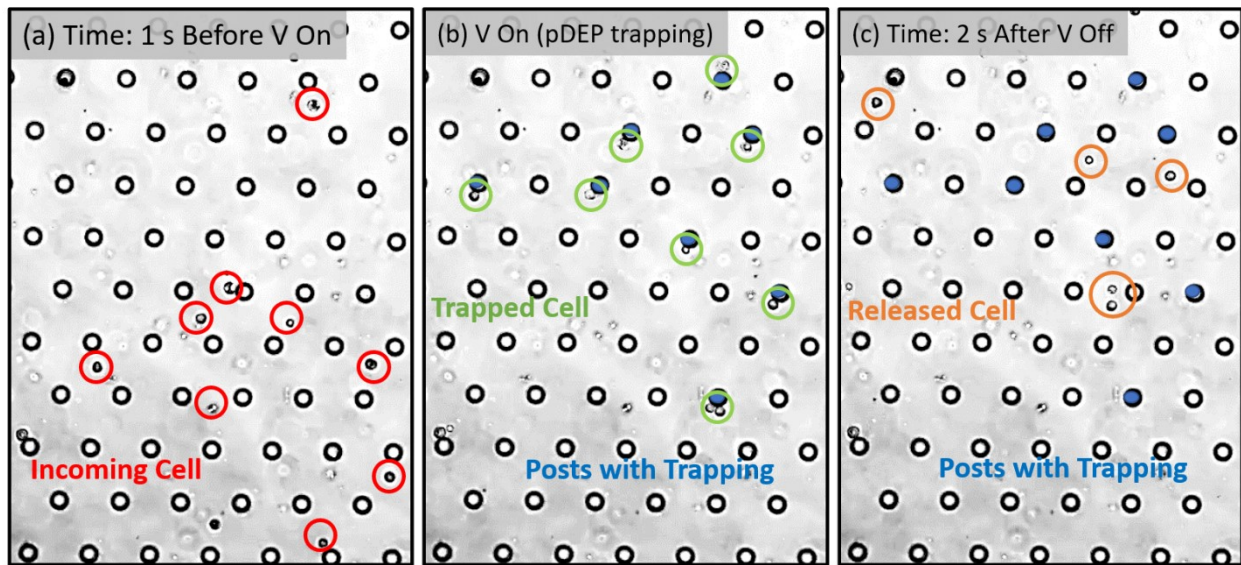


Figure 14: *cDEP* with membrane confined Field's metal electrodes for *pDEP* trapping of macrophages. (a) Incoming cells (circled in red) flowing by inertial 1 second before applying voltage. (b) Cells are trapped (circled in green) at the post (colored in blue) due to *pDEP* at  $400 V_{pp}$  at 80kHz. (c) Cells are released (circled in orange) and moving away from post (colored in blue) by inertial after turning of the voltage.

### **3.2 Continuous Dielectrophoresis**

Continuous DEP separation is the preferred enrichment method to batch DEP separation due to the dynamic control of separation and collection. A major bottleneck that has limited sample throughput in continuous DEP separation is that it requires the cells to be deflected or attracted by a force level greater than its inertia due to fluid flow, so that the deflected cells would be shifted to different flow streamlines for separations into different microchannels and collection. A continuous separation DEP device based on contacted sidewall metal electrodes, orifice device, was realized in this study. Similar to the cDEP devices, the orifice device is comprised of a center channel with two electrode channels on either side, figure 15 (a). The key differences between the cDEP devices and the orifice device is the lack of a physical membrane separating the electrode channel from the sample channel. As discussed in the device design section, Field's metal is used as the activating electrodes, wherein liquid FM was injected into the electrode channels that is contained by a set of orifices on one side of the sample channel and an array of posts on the other, figure 15 (b). In this manner, the planar confined FM electrodes are in direct contact with the sample channel, therefore, resulting in zero voltage loss in the systems, as all the applied voltage to the electrodes are delivered to the sample channel. Microscope images were taken of the active region, figure 16 (a) and single orifices figure 16 (b and c) to validate the fabrication and formation of true 3D electrodes figure 16 (c).

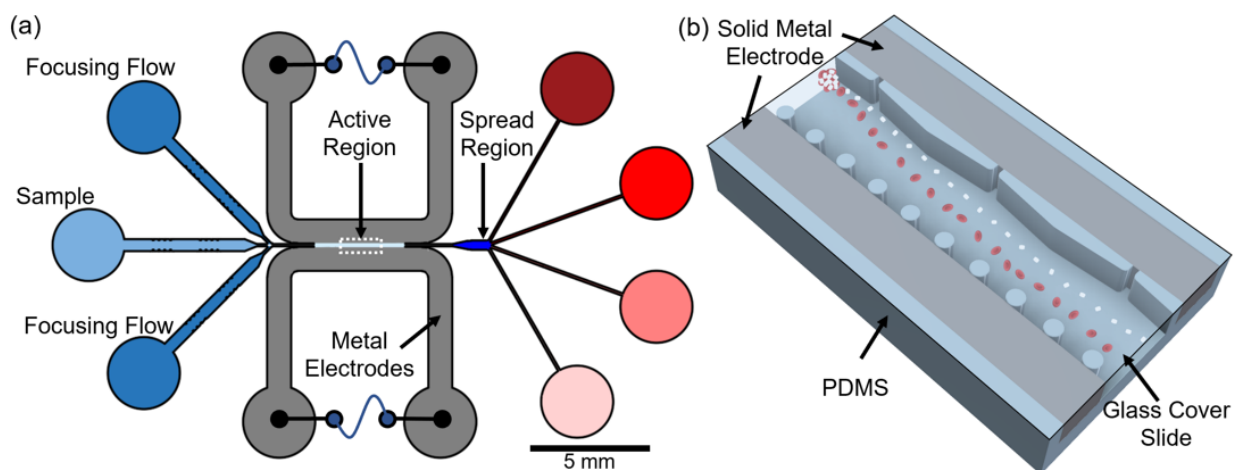


Figure 15. (a) Schematic of the orifice device. (b) Schematic illustrating the 3D aspects of the solidified metal electrodes. Orifices and posts were used to confine the liquid metal during the filling process.

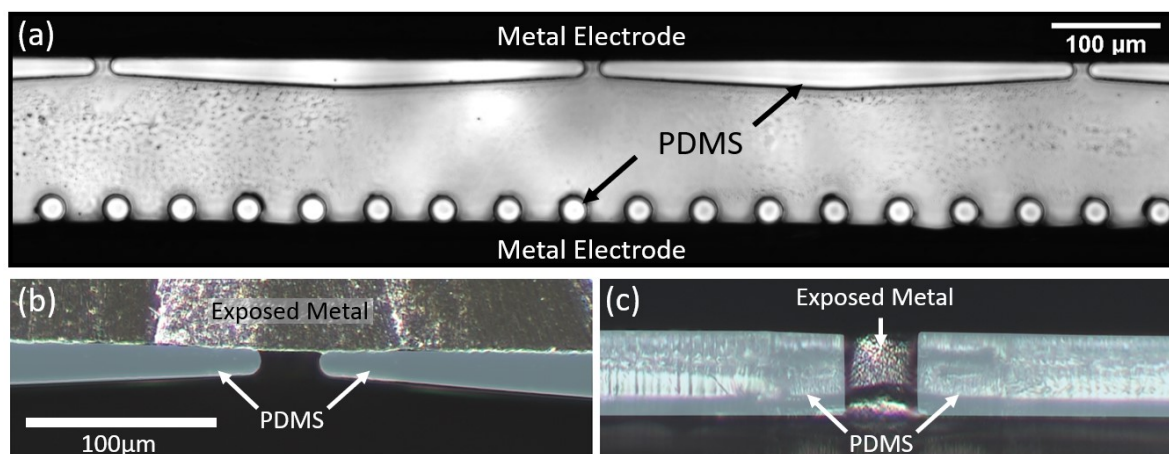


Figure 16: (a) Inverted microscope image of the DEP active region. Optical microscopy of the microfabricated channel with solidified liquid metal, showing the PDMS mold of a single orifice with a filled (b) electrode channel. (c) Cross-section view of an orifice with exposed metal (should this go here or in the device design)

A limiting factor for high throughput continuous DEP separation is the inability to produce an electric field over a high spatial extent (channel depth for instance), without substantially increasing the applied voltage that can cause electrical lysis of the cells. This has been especially challenging for traditional DEP devices with planar electrodes, as the high field point is only located at either the top or bottom of the microchannel. Not only does this traditional electrode

configuration lack the ability to modulate the field across the width of the sample channel, but the limited field extent also becomes more apparent as the sample channel increase in depth. The orifice device presented here is designed and fabricated to have solid metal sidewall electrodes, which creates field non-uniformity across the width of the sample channel and the physical sidewall architecture extends the field non-uniformity along the entire depth of the sample channel. Not only does the sidewall electrode architecture create field non-uniformities in the depth direction, but the field non-uniformities in the x-y plane are maintained. Hence, cells that are dispersed along the depth of the sample channel, z direction, will experience a similar level of DEP force, regardless of their lateral (z) position.

### **3.3 Sidewall Electrodes COMSOL Simulation**

Comsol Multiphysics simulation was used to highlight the 3D field profile of planar electrode and the sidewall metal electrode configuration. To do so, a representative device with the same active regions as the orifice device, but with planar electrode was designed. The planar electrodes are placed at the top rather than bottom of the microchannel to enhance the field visibility in the simulation. A standard alignment precision of  $5\mu\text{m}$  protrusion from the planar electrode into the sample channel was assumed for the geometry used in this model. The respective three-dimensional models were made in AutoCAD with a single orifice and imported to Comsol. Following this, Comsol's electric current module was used to show the 3D electric field profile at the orifice. For this demonstration, electrical property inputs and fluid parameters specific to nDEP were selected as the simulation condition for both configurations. A  $150\text{V}_{\text{pp}}$  at  $40\text{kHz}$  AC voltage was applied to the electrodes flanking the sample channel. An aqueous medium with an electrical conductivity of  $700\ \mu\text{S}/\text{cm}$ , physiological conductivity, was used as the fluid medium coupling the two electrodes. A free triangular mesh was generated with varying element sizes, wherein the area

around the active region has elements that are an order of magnitude smaller than the orifice size. Stationary study was selected to simulate the 3D field profile in two electrode configurations, figure 17 (a and b). To verify the lateral field profile, a 2D surface plot was extracted from the center of the orifice, figure 17 (c and d). The two electrode configurations result in a similar field magnitude non-uniformity near the top surface, upper most in the z direction, however the field in the planar configuration shows a rapid drop in field non-uniformity as the channel extends away from the top surface. Unlike the planar electrode configuration, the sidewall electrode configuration shows the field is uniformly distributed along the depth of the channel.

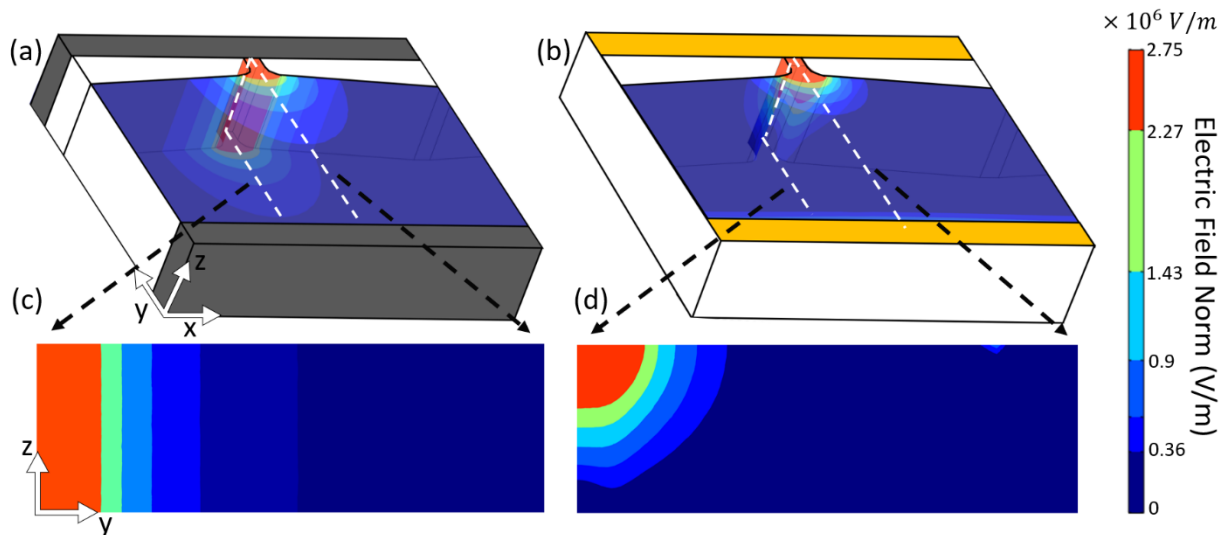


Figure 17: 3D Comsol simulation of electric field norm. Isometric view of a single orifice with (a) 3D and (b) planar electrodes. 2D surface plots taken from a slice at the center of the orifice (white box) from the (c) 3D and (d) planar case.

To further the analysis of 3D and planar electrodes, particle tracing was added to the simulation to demonstrate particle deflection profile. To do so, full channels were added to the single orifice in both 3D and planar electrodes. Particle tracing module was added to the simulation and coupled with the electric current and fluid flow module. Model particles that resemble red blood cells<sup>24,25</sup> were used to study its deflection under nDEP. The list of simulation parameters and properties are

shown in table 1. Similarly, 150Vpp at 40kHz AC voltage was applied to the electrode flanking the sample channel. As shown in figure 18 (a), all the particles traveling in the x direction are deflected upon entering the active region, where the orifice is located. Due to the 3D field that extends along the depth of the channel, particles in any z position are deflected, figure 18 (b). In contrast, particles in the planar electrode case were not sufficiently deflected in the active region despite under the same electrical simulation condition figure 18 (b). In addition, to the particles not deflecting in the correct direction, the particles were deflected in the z direction figure 18 (d). This z direction deflection is the effect of having a localized high field region at the top surface of the microchannel.

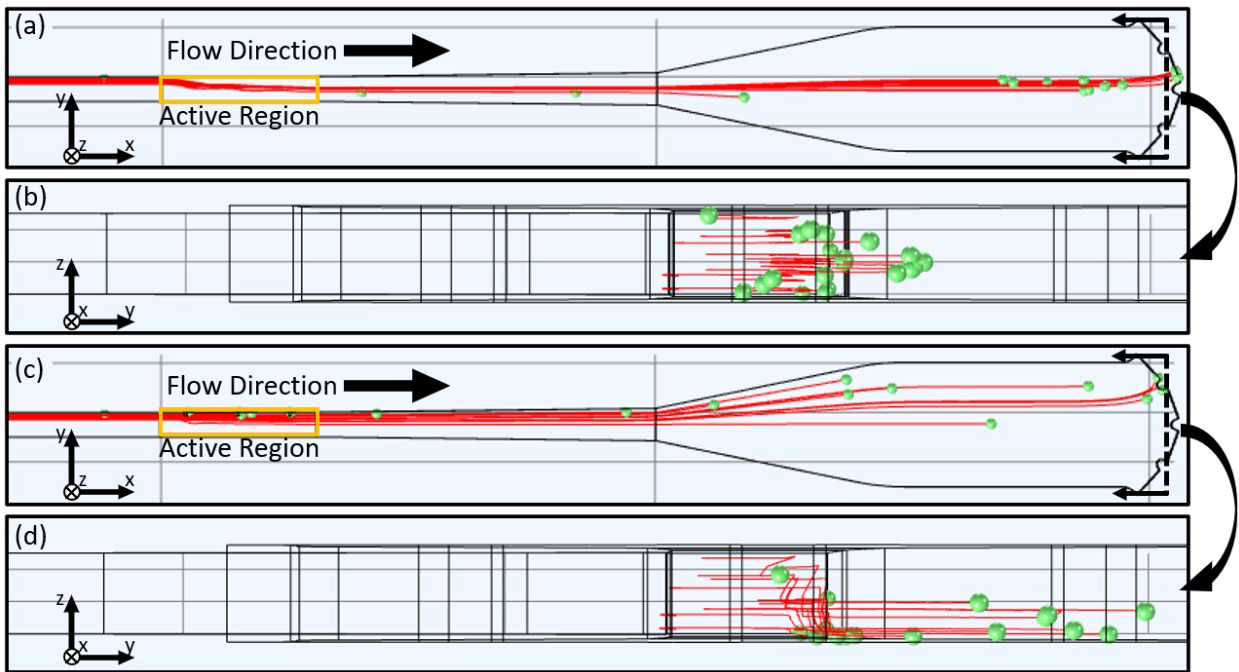


Figure 18: Particle tracing simulation showing nDEP deflection of model particles with (a,c) 3D and (b,d) planar electrodes. (a,b) Top view and (b,d) cross section of the deflected particles' profile.

Parameters and Properties	Values
<b>Operation Parameters</b>	
V <sub>AC</sub> Input	150 V <sub>pp</sub>
Frequency (nDEP)	40 kHz
Normal Inflow Velocity	$3 * 10^4 \mu\text{m}/\text{s}$
<b>Fluid Properties*</b>	
Fluid Medium Conductivity (nDEP)	$700 \mu\text{S}/\text{cm}$
Fluid Density	$1000 \text{ kg}/\text{m}^3$
Fluid Dynamic Density	$1 * 10^{-3} \text{ Pa} * \text{s}$
<b>Particle Properties<sup>22,23</sup></b>	
Particle Diameter (RBCs)	$5 \mu\text{m}$
Shell Thickness (RBCs)	$9 \text{ nm}$
Shell Electrical Conductivity (RBCs)	$1 * 10^{-6} \text{ S}/\text{m}$
Particle Conductivity (RBCs)	$0.31 \text{ S}/\text{m}$
Shell Relative Permittivity (RBCs)	4.44
Particle Relative Permittivity (RBCs)	50

Table 1: Comsol simulation parameters and properties. \*Fluid properties are from COMSOL built-in materials library. Particle properties

### 3.3 Sidewall Electrodes Dielectrophoresis Validation

Since the orifice device is an original design, its frequency selectivity performance was validated by determining the membrane capacitance of red blood cells (RBCs) at different fluid media conductivities. The validation was done by determining the RBCs' crossover frequency at three different media conductivities:  $280 \mu\text{S}/\text{cm}$ ,  $450 \mu\text{S}/\text{cm}$ , and  $720 \mu\text{S}/\text{cm}$ . The conductivities were measured by three independent measurement with a conductivity meter. The RBCs used in this study were from a stock solution of blood type A+ human RBCs diluted to a concentration of  $1.13\text{E}8 \text{ cells}/\text{mL}$ . The RBCs were washed three times and resuspended in a DEP buffer, composed of: 8% sucrose, 1% BSA, and 1X PBS adjusted to the three conductivities mentioned above. The RBCs sample was injected into the sample channel via a syringe and allowed to reach steady state, wherein the cells completely occupy the sample the channel and moving by inertial forces only. A constant  $80\text{V}_{\text{pp}}$  was delivered to the electrodes by a function/arbitrary waveform generator coupled with an amplifier. The cells were imaged with a CMOS camera connected to an inverted

microscope. The crossover behavior was defined as where both nDEP and pDEP was present at a set frequency. The membrane capacitance was then calculated from the media conductivity,  $\sigma_s$ , radius of the particle,  $r$ , and crossover frequency  $f_{CO}$  with the following equation<sup>16,26</sup>.

$$C_{mem} = \frac{\sigma_s}{\sqrt{2\pi r f_{CO}}} \quad (7)$$

A membrane capacitance of  $11.13 \pm 1.28$  mF/m<sup>2</sup> was calculated from the values in table 2, which is to close RBC membrane capacitance shown in prior works<sup>27,28</sup>; hence validating the orifice device's ability for frequency selective cell deflection and attraction.

Media Conductivity ( $\mu\text{s/cm}$ )	Membrane Capacitance (mF/m <sup>2</sup> )
720	10.8
450	10.13
280	12.6

*Table 2: Membrane Capacitance of healthy RBCs at different media conductivities with a mean of 11.13 mF/m<sup>2</sup> and a standard deviation of 1.28 mF/m<sup>2</sup>. Membrane capacitance was calculated from equation Eq 7*

Continuous flow DEP experiments were carried out to demonstrate the continuous dielectrophoretic deflection capability of the orifice device. A low conductive media of 280  $\mu\text{s/cm}$  was chosen to show nDEP at low frequencies and pDEP at high frequencies. To benchmark the sample throughput of the device, a high conductive media of 570  $\mu\text{s/cm}$  was used as higher media conductivity results in higher nDEP force. Similar to the prior sample preparation, the RBCs from the stock solution was diluted to a concentration of  $1.13 \times 10^8$  cells/mL, washed three times and resuspended in the two DEP buffers. Two syringe pumps, a sample syringe and a buffer syringe, were used to fill the sample channel with the desired DEP buffer. The sample syringe was loaded with the RBCs sample and used only for delivering the sample from the sample inlet into the

sample channel. The buffer syringe was comprised of only the DEP buffer and was used to deliver fluid flow from the focusing inlet into the sample channel for hydrodynamic focusing. The purpose of the hydrodynamic focusing is to force the RBCs close to the orifices so that it will experience the optimal DEP force. The voltage to the electrodes were delivered in the same fashion as the prior setups. Post processing and corresponding cell position measurements were made with ImageJ.

At a media conductivity of  $280 \mu\text{s}/\text{cm}$ , the RBCs flowing at a total flow rate of  $0.24 \mu\text{l}/\text{min}$  exhibit a displacement of  $\sim 30 \mu\text{m}$  away from the orifices from its original focusing position under nDEP with the application of  $80V_{\text{pp}}$  at  $30 \text{ kHz}$ , figure 19 (a,b). In the same media and flow rate condition, a displacement of  $\sim 10 \mu\text{m}$  towards the orifices was from its initial streamline was seen under pDEP with supplication of  $80V_{\text{pp}}$  at  $1\text{MHz}$  figure 19 (c,d). The two net displacements under nDEP and pDEP, away and towards the orifices, respectively, enables facile collection of cells in different outlets from the sample channel based on their DEP response. The media conductivity was increased to  $570 \mu\text{s}/\text{cm}$  to demonstrate the maximum flow rate that still enables DEP. A  $\sim 30 \mu\text{m}$  displacement under nDEP was observed when flowing the RBCs at a total flow rate of  $12 \mu\text{l}/\text{min}$  with  $100V_{\text{pp}}$  at  $40\text{kHz}$ , figure 19 (e,f). Despite the 50-fold increase in flow rate compared to that of used with the  $280 \mu\text{s}/\text{cm}$  sample, the DEP deflection shows equivalent levels of net displacement therefore validating our design for high throughput separation strategies of up to  $6.78\text{E}5$  cells/min.

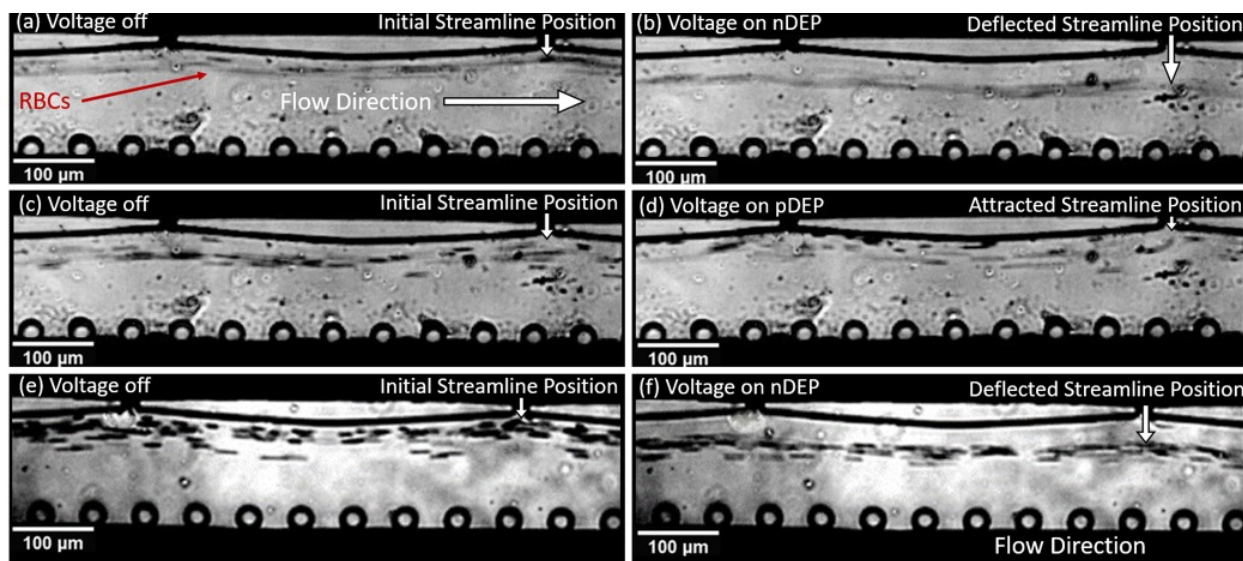


Figure 19: AC DEP on RBCs in 280us/cm buffer solution flowing at 0.24ul/min. (a,c) Initial streamline position with no voltage. (b) nDEP at 30kHz and (d) pDEP at 1MHz  $V = 80V_{pp}$ . (e,f) DEP of RBCS in 540us/cm flowing at 12ul/min with 100Vpp at 40kHz.

## Chapter 4

### In Channel Electrodeposition and Electrochemistry

As stated in the introduction, there are a number of electrochemical sensing applications that would benefit from integrating sidewall electrodes into the microchannel. However, three dimensional electrodes made from AgPDMS, eutectic gallium indium, or Field's metal are not suitable for electrochemical sensing, due to high redox potentials for common molecules. Gold, on the other hand, is the most common working electrode material in electrochemistry applications, but creating gold sidewall electrodes require glancing angle deposition systems. To overcome such challenges, we present a method for forming gold sidewall electrodes in a cleanroom free setting, by carrying out gold electrodeposition inside of a microchannel.

The quality of the electrodeposited gold film is highly sensitive to sensitive to topography and surface area of the active. Therefore, planar confinement of FM using orifices or post was not suitable, as large exposed FM surfaces cannot be well-controlled during fabrication due to interruptions along the length of the microchannel. However, depth confined FM using a step high difference between the sample channel and the electrode channel creates a straight uninterrupted sidewall electrode where the surface area can be calculated with a high level of precision.

To create the gold sidewall electrode, a novel in channel electrodeposition method was developed. First double layer SU-8 and PDMS was used to fabricate the depth confined device with a sample channel of 50 $\mu\text{m}$  and electrode channel of 100 $\mu\text{m}$ . Rather than using the FM as the simulating electrode, the FM was used as a sidewall architecture, wherein the exposed surface would be electrodeposited with gold. To characterize the depth confinement of FM, optical microscopy of cross-section view of the depth confined Field's metal in PDMS were taken, figure 20. It can be

seen that exposed metal edge extends the entire channel depth (50 $\mu$ m) and spans the 300 $\mu$ m along the length of the sample channel without interruptions.

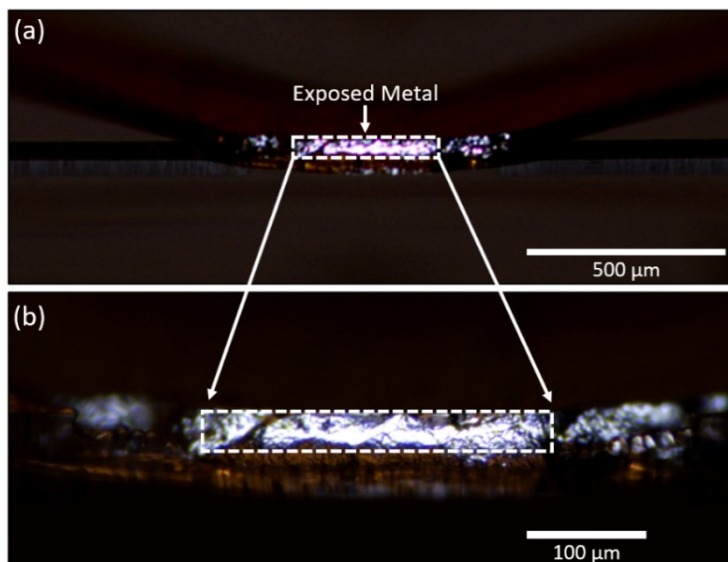


Figure 20: Optical microscopy of cross-section view of the depth confined Field's metal in PDMS

The electrode deposition was done in gold bath comprised of: (34.7mM  $\text{KAu}(\text{Cn})_2$ , 0.208 M citric acid, and 0.177 M Ammonium citrate dibasic) adjusted to a pH of 3.8. A pipette was used to fill the sample channel with the gold bath. Macro reservoirs were made to interface with the inlet and outlet of the sample channel so that a Pt wire counter electrode and Ag/AgCl in 3M KCl reference electrodes could be inserted into the reservoirs, figure 21.

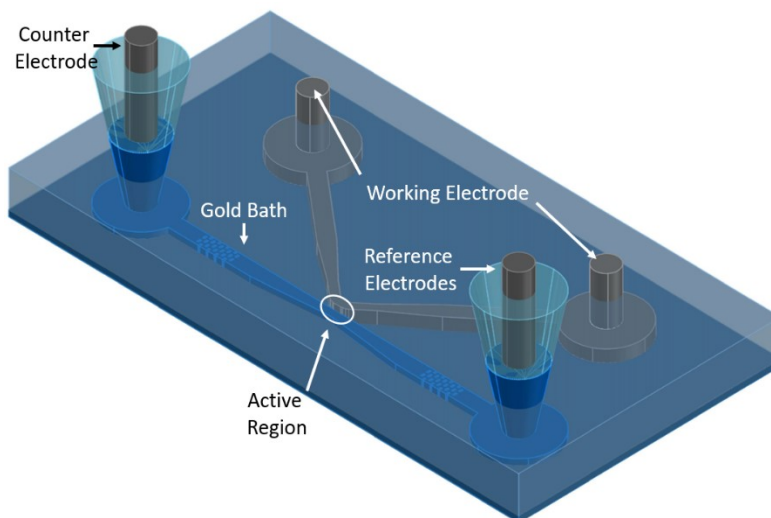


Figure 21: Schematic of gold electrodeposition on Field's metal in a microchannel

Prior to deposition, an open circuit potential was measured for 120 seconds to ensure the electrical connections are stable and with an absence of bubbles in the sample channel. A chronopotentiometry at  $-3E-6A$  was run for 1500 seconds, as the deposition step to create a thin layer of gold on the FM. After the deposition, the sample channel was rinsed with DI water and dried via vacuum. To validate the in-channel gold deposition, a CV with ferrocyanide was performed inside of the microchannel in fashion similar to deposition set up. First, a CV was done on bare Field's metal to show the lack of redox potential figure 22 (a). CVs were then done with the gold coated FM inside of a channel and on a gold wafer as bench mark, figure (b and c). Despite the weak oxidation and reduction peaks from the gold coated FM in figure 22 (b) compared to that of a gold wafer figure 22 (c), the gold coated FM clearly shows EC sensing capabilities compared with that of bare Field's metal, figure 22 (a).

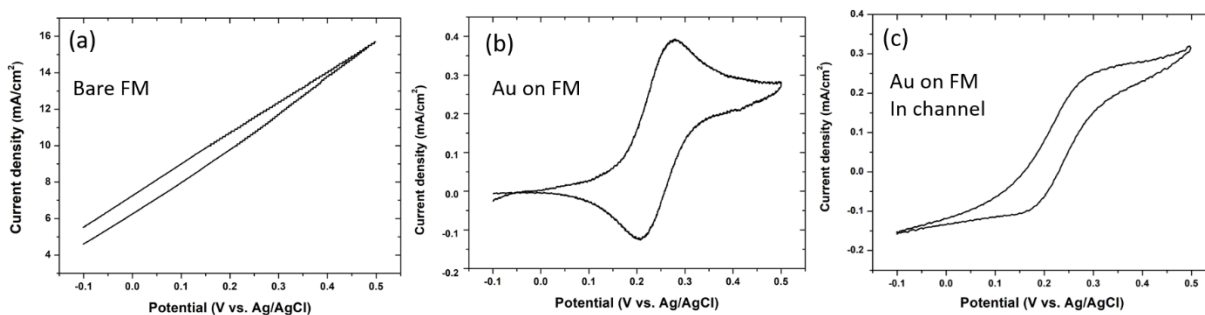


Figure 22: EC sensing of Ferricyanide for validation Cyclic voltammograms (CV) of (a) gold coated Field's metal electrode inside a microchannel (b) bare field's metal electrode outside of channel and (c) gold wafer in  $2\text{ mM } K_3[Fe(CN)_6] + 0.1\text{ M } KCl$  solution

## Chapter 5

### Conclusion and Future outlook

Novel sidewall metal electrode fabrication methods for microfluidics were explored with Field's metal in this study. The chief principle is based on a co-fabrication strategy, wherein liquid metal is filled into a confined microchannel to be the electrode channel. Three electrode confinement methods were examined here: membrane confinement, planar confinement, and depth confinement. Each confinement method, figure 10, was used to fabricate devices for the following applications contactless DEP, continuous DEP, and in-channel electrochemistry.

Replacing the liquid electrodes in existing cDEP devices with liquid metal electrodes increased device fabrication reproducibility and device durability. As discussed in chapter 3, cDEP devices have had low reproducibility due to the long and thin insulative membrane separating the electrode channels from the sample channel. Having a pristine membrane in prior cDEP devices was crucial since any imperfections would result in the conductive liquid (10X PBS) electrodes leaking from the electrode channels into the sample channel; therefore, rendering the device faulty as pDEP cannot be realized at a media conductivity similar to that of 10X PBS. With membrane confinement, the electrode channels were filled with liquid metal, such as FM, and allowing it to solidify at room temperature overcomes the pristine membrane requirement during fabrication. The high viscosity of liquid FM can be retained in the electrode channel despite membrane imperfections, therefore recovering devices with defects up to 70 $\mu$ m in length. In addition to recovering imperfect devices, solidified FM acts as a physical reinforcement to the membrane, so that the device has higher durability during operation and increases shelf stability. Unlike the case of 10X PBS that can evaporate or crystallize in the electrode channel, FM is stable at room

temperature. pDEP trapping of macrophages in a buffer of buffer of  $25\mu\text{S}/\text{cm}$  media conductivity at  $400V_{pp}$  at  $80\text{kHz}$  was shown with FM electrodes replaced cDEP devices to validate its operation. The cDEP devices here were made from PDMS which is not viable for commercialization, therefore, future studies should examine integrating Field's metal as electrodes in other materials commonly found in microfluidics such as cyclic olefin copolymer (COC), Polymethyl methacrylate (PMMA), and SU-8 on glass.

As discussed in chapter 1, the throughput of continuous DEP separation has been low due to the poor field coupling and fabricating sidewall electrodes requires highly specialized metal deposition tools. With planar confinement, we demonstrated facile fabrication techniques and design parameters to create field non-uniformities that extends the entire depth and across the width of the microchannel. As detailed in chapter 3, the liquid FM was injected into the electrode channels and was confined by a set of posts on one side and a set of orifices on the other. The orifice and post geometry shown in figure 15 (a) creates the field non-uniformity across the sample channel to enable DEP response. In addition to the solid metal edges, the high field points are patterned sequentially for progressive DEP deflection. The novel orifice device, figure 14 (a), was validated for frequency selective DEP manipulation by determining red blood cells' crossover at a low, medium, and high conductive media, resulting in a computed RBC membrane capacitance of  $11.13\pm 1.28\text{ mF}/\text{m}^2$ . Continuous nDEP and pDEP was demonstrated with RBCs at a sample flow rate of  $0.24\mu\text{L}/\text{min}$  in a buffer of  $280\mu\text{S}/\text{cm}$  media conductivity. nDEP deflection of net displacement of  $\sim 30\mu\text{m}$  from its original streamline was seen at  $80V_{pp}$  at  $30\text{kHz}$  and pDEP attraction of net displacement of  $\sim 10\mu\text{m}$  from its original stream line was seen at  $80V_{pp}$  at  $1\text{MHz}$ . To benchmark the throughput of the orifice device, RBCs in a  $570\mu\text{S}/\text{cm}$  buffer flowing at  $12\mu\text{L}/\text{min}$  were deflected  $\sim 30\mu\text{m}$  from its original streamline under nDEP at  $100V_{pp}$  at  $40\text{kHz}$ ;

thereby demonstrating a high sample throughput of  $6.78E5$  cells/min. Beyond deflecting RBCs, more complicated cell types such as stem cells and cancer cell should be tested with the orifice device. Future more, orifice geometry should be studied in depth, such that smaller particles such as bacteria or even extracellular vessels could be separated. To take full advantage of the continuous separation, real time on-chip downstream sample or media analysis should be explored. The analysis can include on-chip single cell impedance cytometry, thereby eliminating excess cell handling following separation, and on-chip media conductivity measurement following DEP separation such that media quality can be monitored.

Depth confinement of liquid metal was explored to enable electrochemistry on a sidewall electrode in a microchannel. Unlike planar confinement, depth confined liquid metal create an uninterrupted sidewall electrode with a well-defined exposed surface so that the active area for electrodeposition and sensing can be calculated to a high degree. In this study, a step height between the sample and electrode channel was explored to create the depth confinement of liquid FM. Upon creating a continuous solid metal sidewall electrode, the architecture acts as a substrate for in channel electrodeposition of gold on the sidewall surface. Cyclic voltammetry was performed inside the microchannel with the gold sidewall electrode to validate gold's oxidation and reduction peaks in ferrocyanide. The realization of a cleanroom free fabrication method to create gold sidewall electrodes capable of biosensing opens a plethora of integrated microfluidic applications that takes advantage precise flow control such as hydrodynamic focusing and diffusive mixing.

## References

- (1) Aryasomayajula, A.; Bayat, P.; Rezai, P.; Selvaganapathy, P. R. Microfluidic Devices and Their Applications. In *Springer Handbook of Nanotechnology*; Bhushan, B., Ed.; Springer Handbooks; Springer: Berlin, Heidelberg, 2017; pp 487–536. [https://doi.org/10.1007/978-3-662-54357-3\\_16](https://doi.org/10.1007/978-3-662-54357-3_16).
- (2) Craighead, H. Future Lab-on-a-Chip Technologies for Interrogating Individual Molecules. *Nature* **2006**, *442* (7101), 387–393. <https://doi.org/10.1038/nature05061>.
- (3) Convery, N.; Gadegaard, N. 30 Years of Microfluidics. *Micro and Nano Engineering* **2019**, *2*, 76–91. <https://doi.org/10.1016/j.mne.2019.01.003>.
- (4) Petchakup, C.; Li, K. H. H.; Hou, H. W. Advances in Single Cell Impedance Cytometry for Biomedical Applications. *Micromachines (Basel)* **2017**, *8* (3). <https://doi.org/10.3390/mi8030087>.
- (5) Wang, X.-B.; Yang, J.; Huang, Y.; Vykoukal, J.; Becker, F. F.; Gascoyne, P. R. C. Cell Separation by Dielectrophoretic Field-Flow-Fractionation. *Anal Chem* **2000**, *72* (4), 832–839.
- (6) Horny, M.-C.; Lazerges, M.; Siaugue, J.-M.; Pallandre, A.; Rose, D.; Bedioui, F.; Deslouis, C.; Haghiri-Gosnet, A.-M.; Gamby, J. Electrochemical DNA Biosensors Based on Long-Range Electron Transfer: Investigating the Efficiency of a Fluidic Channel Microelectrode Compared to an Ultramicroelectrode in a Two-Electrode Setup. *Lab Chip* **2016**, *16* (22), 4373–4381. <https://doi.org/10.1039/C6LC00869K>.
- (7) Hughes, M. P. Fifty Years of Dielectrophoretic Cell Separation Technology. *Biomicrofluidics* **2016**, *10* (3), 032801. <https://doi.org/10.1063/1.4954841>.
- (8) Piacentini, N.; Mernier, G.; Tornay, R.; Renaud, P. Separation of Platelets from Other Blood Cells in Continuous-Flow by Dielectrophoresis Field-Flow-Fractionation. *Biomicrofluidics* **2011**, *5* (3), 034122–034122–034128. <https://doi.org/10.1063/1.3640045>.
- (9) Torres-Castro, K.; Honrado, C.; Varhue, W. B.; Farmehini, V.; Swami, N. S. High-Throughput Dynamical Analysis of Dielectrophoretic Frequency Dispersion of Single Cells Based on Deflected Flow Streamlines. *Anal Bioanal Chem* **2020**, *412* (16), 3847–3857. <https://doi.org/10.1007/s00216-020-02467-1>.
- (10) Cofabrication: A Strategy for Building Multicomponent Microsystems | Accounts of Chemical Research [https://pubs.acs.org/doi/abs/10.1021/ar900178k?casa\\_token=5qekcKcKZfMAAAAA:WC2\\_S\\_EpsYadiyzYSr5eaXErkvg4tKLWUsOH3a748RH5knocxIK0sM89nW\\_bHg80ic8up1IIdMmZPyjB](https://pubs.acs.org/doi/abs/10.1021/ar900178k?casa_token=5qekcKcKZfMAAAAA:WC2_S_EpsYadiyzYSr5eaXErkvg4tKLWUsOH3a748RH5knocxIK0sM89nW_bHg80ic8up1IIdMmZPyjB) (accessed Mar 8, 2021).
- (11) Salahi, A.; Varhue, W. B.; Farmehini, V.; Hyler, A. R.; Schmelz, E. M.; Davalos, R. V.; Swami, N. S. Self-Aligned Microfluidic Contactless Dielectrophoresis Device Fabricated by Single-Layer Imprinting on Cyclic Olefin Copolymer. *Anal Bioanal Chem* **2020**, *412* (16), 3881–3889. <https://doi.org/10.1007/s00216-020-02667-9>.
- (12) Lewpiriyawong, N.; Yang, C.; Lam, Y. C. Continuous Sorting and Separation of Microparticles by Size Using AC Dielectrophoresis in a PDMS Microfluidic Device with 3-D Conducting PDMS Composite Electrodes. *ELECTROPHORESIS* **2010**, *31* (15), 2622–2631. <https://doi.org/10.1002/elps.201000087>.
- (13) So, J.-H.; Dickey, M. D. Inherently Aligned Microfluidic Electrodes Composed of Liquid Metal. *Lab Chip* **2011**, *11* (5), 905–911. <https://doi.org/10.1039/C0LC00501K>.
- (14) Pethig, R. Review Article—Dielectrophoresis: Status of the Theory, Technology, and Applications. *Biomicrofluidics* **2010**, *4* (2), 022811. <https://doi.org/10.1063/1.3456626>.
- (15) Sun, M.; Agarwal, P.; Zhao, S.; Zhao, Y.; Lu, X.; He, X. Continuous On-Chip Cell Separation Based on Conductivity-Induced Dielectrophoresis with 3D Self-Assembled Ionic Liquid Electrodes. *Anal Chem* **2016**, *88* (16), 8264–8271. <https://doi.org/10.1021/acs.analchem.6b02104>.

- (16) Gascoyne, P. R. C.; Shim, S.; Noshari, J.; Becker, F. F.; Stemke-Hale, K. Correlations between the Dielectric Properties and Exterior Morphology of Cells Revealed by Dielectrophoretic Field-Flow Fractionation. *Electrophoresis* **2013**, *34* (7), 1042–1050. <https://doi.org/10.1002/elps.201200496>.
- (17) Bakker, E.; Telting-Diaz, M. Electrochemical Sensors. *Anal. Chem.* **2002**, *74* (12), 2781–2800. <https://doi.org/10.1021/ac0202278>.
- (18) Zhao, K.; Larasati; Duncker, B. P.; Li, D. Continuous Cell Characterization and Separation by Microfluidic Alternating Current Dielectrophoresis. *Anal. Chem.* **2019**, *91* (9), 6304–6314. <https://doi.org/10.1021/acs.analchem.9b01104>.
- (19) Čemažar, J.; Douglas, T. A.; Schmelz, E. M.; Davalos, R. V. Enhanced Contactless Dielectrophoresis Enrichment and Isolation Platform via Cell-Scale Microstructures. *Biomicrofluidics* **2016**, *10* (1), 014109. <https://doi.org/10.1063/1.4939947>.
- (20) Farmehini, V.; Varhue, W.; Salahi, A.; Hyler, A. R.; Čemažar, J.; Davalos, R. V.; Swami, N. S. On-Chip Impedance for Quantifying Parasitic Voltages During AC Electrokinetic Trapping. *IEEE Transactions on Biomedical Engineering* **2020**, *67* (6), 1664–1671. <https://doi.org/10.1109/TBME.2019.2942572>.
- (21) Niu, X. Z.; Peng, S. L.; Liu, L. Y.; Wen, W. J.; Sheng, P. Characterizing and Patterning of PDMS-Based Conducting Composites. *Advanced Materials* **2007**, *19* (18), 2682–2686. <https://doi.org/10.1002/adma.200602515>.
- (22) Hoettges, K. F.; Henslee, E. A.; Torcal Serrano, R. M.; Jabr, R. I.; Abdallat, R. G.; Beale, A. D.; Waheed, A.; Camelliti, P.; Fry, C. H.; van der Veen, D. R.; Labeed, F. H.; Hughes, M. P. Ten-Second Electrophysiology: Evaluation of the 3DEP Platform for High-Speed, High-Accuracy Cell Analysis. *Scientific Reports* **2019**, *9* (1), 19153. <https://doi.org/10.1038/s41598-019-55579-9>.
- (23) Chan, J. Y.; Ahmad Kayani, A. B.; Md Ali, M. A.; Kok, C. K.; Yeop Majlis, B.; Hoe, S. L. L.; Marzuki, M.; Khoo, A. S.-B.; Ostrikov, K. (Ken); Aatur Rahman, Md.; Sriram, S. Dielectrophoresis-Based Microfluidic Platforms for Cancer Diagnostics. *Biomicrofluidics* **2018**, *12* (1). <https://doi.org/10.1063/1.5010158>.
- (24) Park, S.; Zhang, Y.; Wang, T.-H.; Yang, S. Continuous Dielectrophoretic Bacterial Separation and Concentration from Physiological Media of High Conductivity. *Lab Chip* **2011**, *11* (17), 2893. <https://doi.org/10.1039/c1lc20307j>.
- (25) Egger, M.; Donath, E. Electrorotation Measurements of Diamide-Induced Platelet Activation Changes. *Biophys J* **1995**, *68* (1), 364–372.
- (26) Gascoyne, P. R. C.; Shim, S. Isolation of Circulating Tumor Cells by Dielectrophoresis. *Cancers (Basel)* **2014**, *6* (1), 545–579. <https://doi.org/10.3390/cancers6010545>.
- (27) Lapizco-Encinas, B. H. On the Recent Developments of Insulator-Based Dielectrophoresis: A Review. *ELECTROPHORESIS* **2019**, *40* (3), 358–375. <https://doi.org/10.1002/elps.201800285>.
- (28) Cottet, J.; Fabregue, O.; Berger, C.; Buret, F.; Renaud, P.; Frénéa-Robin, M. MyDEP: A New Computational Tool for Dielectric Modeling of Particles and Cells. *Biophys J* **2019**, *116* (1), 12–18. <https://doi.org/10.1016/j.bpj.2018.11.021>.